HIGH-LATITUDE PLASMA DRIFT STRUCTURING FROM A FIRST PRINCIPLES IONOSPHERIC MODEL

BY

HEEJIN KIM

Submitted in partial fulfillment of the
requirements for the degree of
Master of Science in Mechanical and Aerospace Engineering
in the Graduate College of the
Illinois Institute of Technology

Approved 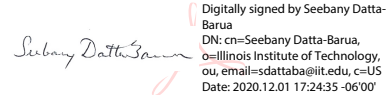

Advisor

Chicago, Illinois
December 2020

ACKNOWLEDGMENT

First and foremost, I would like to express my deep appreciation to my master thesis advisor, Dr. Datta-Barua. I have had many great opportunities since I became Dr. Datta-Barua's student in Space Weather Lab. She continually and convincingly conveyed a sense of insight in regard to research and scholarship, and wisdom of life. I am blessed to have had the opportunity to do research under the professor. Without her guidance and persistent help this dissertation would not have been possible. I would like to extend the thank to my committee members, Dr. Pervan and Dr. Cassel, serving my defense committee, encouraging my process, and reviewing my thesis.

Thank you to all my colleagues at Space Weather Lab, Ningchao Wang, Shahrukh Khan, Roohollah Parvizi, Aurora Lopez, Zachary Bonson, Leanne Nutter, David Stuart, and Li Pan, for sharing knowledge and helping me. Also, thank you to other colleagues and friends outside the lab, who shared my difficulties and encouraged me.

I would also like to thank my parents, Dukki Kim and Heechung Kim. I always appreciate your endless support, love, and sacrifice. Your existence makes me challenge and moves forward.

Special thanks to my grandfather Youngbok Kim and grandmother Kwanok Jun. Although each hug before leaving Korea for the IIT entrance became the last hugs for both of you, you are always deep down in my heart.

TABLE OF CONTENTS

LIST OF FIGURES

ABSTRACT

In the high-latitude ionosphere dense plasma formations called polar cap patches are sometimes observed. These patches are often associated with ionospheric scintillation, a rapid fluctuation in the amplitude and phase of a radio signal that degrades communications and navigation systems. Predicting polar cap patch movement across the polar cap is an important subject for enabling forecasting of the scintillation.

Lagrangian coherent structures (LCSs) are ridges indicating regions of maximum fluid separation in a time-varying flow. In previous studies, the Ionosphere-Thermosphere Algorithm for Lagrangian Coherent Structures (ITALCS) predicted the location of LCSs. These LCSs were shown to constrain polar cap patch source and transport regions for flow assumed to due to $\vec{E} \times \vec{B}$ plasma drift. The LCSs were predicted based on an empirical model of the high-latitude electric field for $\vec{E}$.

In this thesis, the LCSs are generated using the first principles ionospheric model SAMI3 (SAMI3 is Another Model of the Ionosphere) as the model for electric field. The work relies on an understanding of various magnetic coordinate systems in space science, and includes three different approaches for attempting to generate the $\vec{E} \times \vec{B}$ drift as the flow fields that are to input to ITALCS. Finally, a representative LCS result is obtained with SAMI3 and shown to be at the high latitudes on the dayside, similar to prior work, but spanning a shorter longitudinal range.

CHAPTER 1

INTRODUCTION

Plasma is a state of matter containing ionized atoms, molecules, and free electrons. The atmosphere can be classified into several different layers based on its temperature and ionization characteristics. While the thermosphere is neutral, ionized particles, electrically charged ions and free electrons, are created within it from the absorption of extreme ultraviolet and x-rays by neutral atoms and molecules [1]. Even though it has less than 1% ionization, the presence of plasma is significant enough to see the movement of charged particles based on electromagnetic forcing, and is referred to as the ionosphere. The ionosphere ranges in altitude from below 50 km to up to 1000 km and beyond.

Within the ionosphere, the region with the densest plasma is the F2 layer, at an altitude from about 200 km up, shown in Figure 1.1. The ionosphere has important effects on radiowave propagation. The index of refraction is proportional to the plasma density. For higher frequencies, the signal will be trans-ionospheric but will undergo group delay. Sometimes the F layer has rapid or erratic variation in density as compared with a typical smoothly varying density [2], and is sometimes referred to as "sporadic F." The sporadic ionization is often associated with larger (100s of km) regions of high plasma density. In the high latitudes, these density enhancements are referred to as polar cap patches. Polar cap patches are also associated with rapid fluctuations in the amplitude and phase of trans-ionospheric signals such as those of Global Navigation Satellite Systems (GNSS). The fluctuations are called "scintillation" and can degrade position, navigation, and timing service. Knowing where patches convect using a high-fidelity model of the ionosphere could contribute to an effective radio signal degradation forecast system.

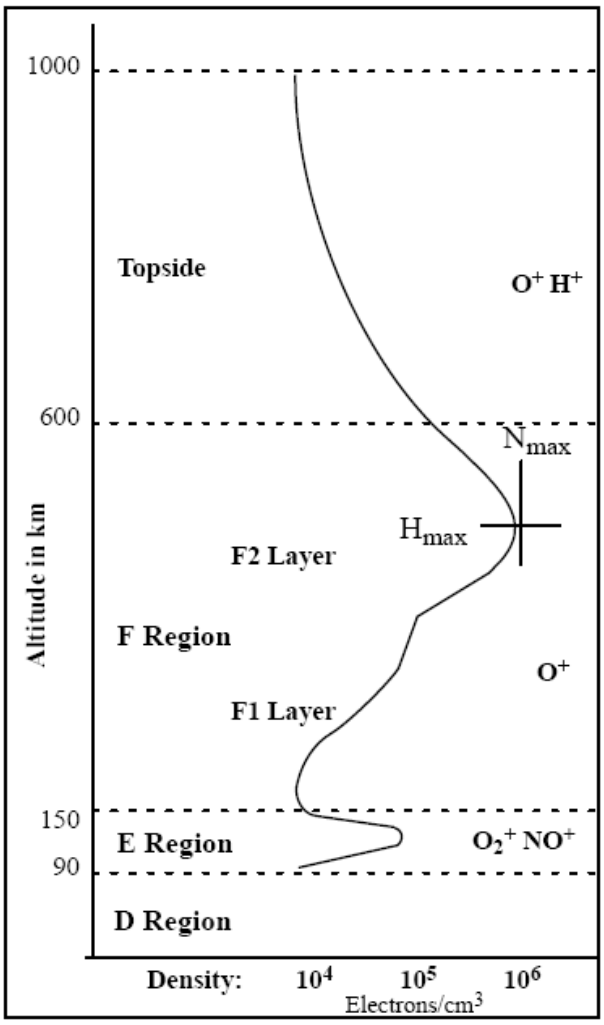

Figure 1.1. Atmospheric layers. The plasma ionosphere is embedded in the neutral thermosphere. The F region is a layer of the ionosphere, and has multiple regions, or layers. The layers' altitude ranges vary from day to night and with the level of activity of the Sun. Credit: Wikimedia commons [3]

1.1 Prior work

In fluid dynamics, one commonly used reference frame for analysis is the Eulerian frame, in which an observer watches fluid moving past. The Lagrangian frame, in contrast, is the one that moves with the fluid. While the Eulerian frame is useful in many contexts, coherent structures identified in the flow as seen in this frame are observer-dependent [4]. In contrast, structures identified in the Lagrangian frame are objective, independent of the observer. These Lagrangian coherent structures (LCSs) are ridges that show maximal separation in a time-evolving flow [5]. Most commonly, LCSs are found by computing the finite-time Lyapunov exponent (FTLE) everywhere in the fluid domain and identifying the locus of points with the locally maximum FTLE as the LCS [6].

To find such structures in the plasma of the ionosphere, past research used the Ionosphere-Thermosphere Algorithm for Lagrangian Coherent Structures (ITALCS) [7]. The LCSs were found to be at high latitudes in a horseshoe shape surrounding the poles with the opening on the night side [8]. The input $\vec{E} \times \vec{B}$ drifts in that paper were calculated from Weimer [9] and International Geomagnetic Reference Field (IGRF-12) [10]. Weimer is a model that uses twin, empirical representations of the ionospheric electric and magnetic Euler potentials' response to the interplanetary magnetic field (IMF) drivers [9]. A follow-on study of ionospheric LCSs used measurements of high-latitude drifts from an array of radars and found the LCSs to be shaped more like a "W" [11].

Empirical models of electric potential such as Weimer [9] do not model the internal physics, and measurement-based convection can require significant extrapolation to regions beyond the measurements (e.g., spanning the high-latitude Russian sector). Both may negatively impact accuracy in the shape and location of the La-

grangian coherent structure.

1.2 Contribution

In this thesis, I use SAMI3 (SAMI3 is Another Model of the Ionosphere), a first principles ionospheric model, to compute LCS ridges. This is the first time applying a first-principles ionospheric model to study LCSs. I investigate three methods for transforming the flow field vectors in order to obtain the LCSs, the third of which is used for analyzing LCSs as modeled by SAMI3. This research will lead to analysis and prediction of polar cap patch movement.

CHAPTER 2
BACKGROUND

2.1 $\vec{E} \times \vec{B}$ drift

In this section, I review how single charged particle motion can give rise to bulk plasma drift in the presence of both electric and magnetic fields. If we consider the external force on a charge q due to an electrostatic field $\vec{E}$ only:

$$\vec{F} = q\vec{E} \tag{2.1}$$

the charge will accelerate in the direction of the field. If this is the only force acting on the charge, the charge q with mass m will accelerate along the direction of the field:

$$\vec{a} = \frac{q}{m}\vec{E} \tag{2.2}$$

A charge moving at velocity $\vec{v}$ in the presence of only a magnetic field $\vec{B}$ is subject to the force:

$$\vec{F} = q\vec{v} \times \vec{B} \tag{2.3}$$

where $\vec{v}$ is the charged particle's velocity, and $\vec{B}$ is the magnetic field. For a positively charged particle moving in the $\hat{x}$ direction with uniform magnetic field directed along $\hat{y}$, a positive charge undergoes a force in the $\hat{z}$ direction. Since the force is always perpendicular to the velocity vector, the charge will undergo circular motion in the plane normal to the field. An electron will circle in the opposite sense from an ion. This circular motion is called gyration [12]. A particle's velocity component along the field line is unchanged by the magnetic field. A particle with nonzero velocity along the field line will "corkscrew" around it but will remain confined to that field line.

The radius of gyration r_g can be found by equating the $\vec{v} \times \vec{B}$ force with the centripetal force:

$$\frac{mv_\perp^2}{r_g} = |q|v_\perp B \tag{2.4}$$

$$r_g = \frac{mv_\perp}{|q|B} \tag{2.5}$$

where the $\perp$ symbol indicates the component orthogonal to $\vec{B}$. Note that as the speed perpendicular to the magnetic field $v_\perp$ increases, the radius of gyration increases.

When both electric and magnetic fields are present, the sum of Eqs. (2.3) and (2.1) is the Lorentz force

$$\vec{F} = q(\vec{E} + \vec{v} \times \vec{B}) \tag{2.6}$$

If the electric field has a component orthogonal to the magnetic field, the electric field causes the charge to change speed $v_\perp$ perpendicular to the magnetic field. Thus, the radius of gyration changes. The net motion as a result of gyration with a varying radius is a drift of the the center of the gyration. The drift vector is in a direction perpendicular to both the electric field and the magnetic field (see Figure 2.1). The particle will undergo a net drift. This "E cross B" drift is given by:

$$\vec{v}_E = \frac{\vec{E} \times \vec{B}}{B^2} \tag{2.7}$$

The $\vec{E} \times \vec{B}$ drift is independent of charge. Therefore, electrons and ions drift in the same direction at the same speed, resulting in no net current [12].

In the ionosphere, plasma is subject to electric fields and the Earth's geomagnetic field. In the high-latitude ionosphere $\vec{E} \times \vec{B}$ drift is significant. In the F layer the plasma flow can be assumed to be entirely $\vec{E} \times \vec{B}$. At lower altitudes which have a higher density of neutral particles, neutral winds and collisional effects also matter. The typical high latitude $\vec{E} \times \vec{B}$ drift pattern consists of two cells of circulation. Plasma drifts from the noon longitude over the pole to midnight, then some plasma

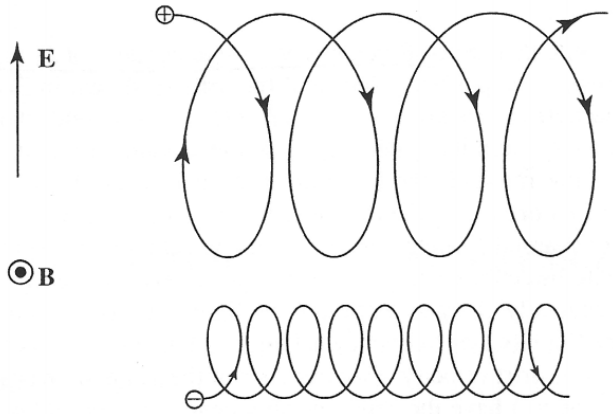

Figure 2.1. Particle drifts in crossed $\vec{E}$ and $\vec{B}$ fields. The negatively charged particle is assumed to have the same velocity as the positively charged one but a smaller mass and therefore a smaller gyro radius. The $\vec{E} \times \vec{B}$ drift speed $\vec{v_E}$ for both particles is the same. Credit: Bittencourt [13]

circulates around to the dawn longitude back to noon, and other plasma flows around to the dusk longitude back to noon, at high magnetic latitudes.

To obtain $\vec{E} \times \vec{B}$ drift we need to know the external electric field and magnetic field. Electric field $\vec{E}$ can be found as the negative gradient of a scalar electric potential function V_E, with units of Volts:

$$\vec{E} = -\vec{\nabla} V_E \tag{2.8}$$

2.2 Magnetic field

Several model representations of Earth's internally generated magnetic field are common. The simplest is the centered dipole model, in which the magnetic field is represented as that of a magnetic dipole (e.g., a bar magnet), as illustrated in Figure 2.2. Magnetic field lines point toward the Arctic, which means that what we call the magnetic north pole is actually the south end of the "bar magnet" of Earth.

Every magnetic field line has a maximum radius from the center of Earth R_{eq}

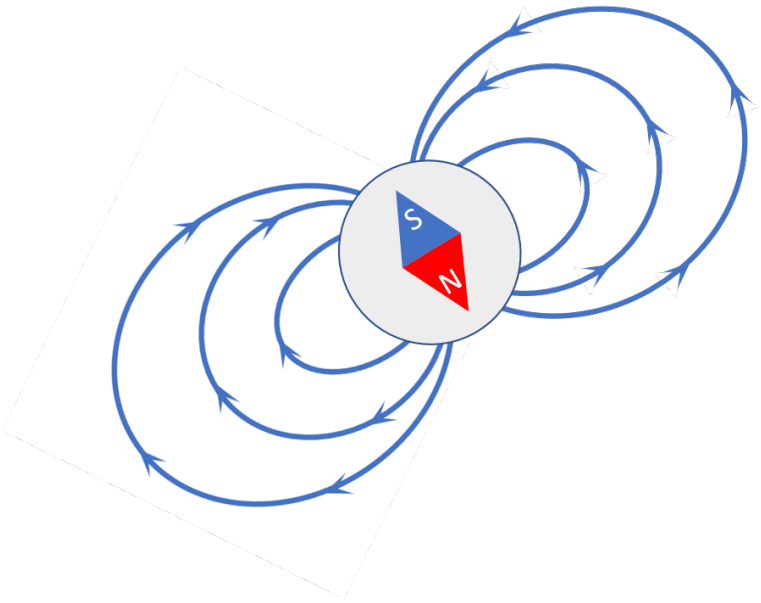

Figure 2.2. Illustration of magnetic field lines. Magnetic field around the earth when we consider the earth as a simple dipole magnet drawn in its center.

at the magnetic equator.

$$r = R_{eq} \cos^2 \lambda_m \tag{2.9}$$

where λ_m is the magnetic latitude measured from the equatorial plane of the magnetic dipole axis. The radius R_{eq} can be used to refer to the set of field lines or "shell" all having that same equatorial radius. This is known as the "L-shell." The equation for the L-shell is:

$$r = L \cos^2 \lambda_m \tag{2.10}$$

where r is the radial distance in units of Earth radii R_E to a point on the line, and L is the L-shell in units of Earth radii.

An even more accurate model of the Earth's internal magnetic field, called the "eccentric dipole," is one for which the dipole axis does not pass through the center of Earth. Instead the dipole center is offset from the center of Earth in the direction of east Asia. The primary effect of the eccentric dipole is that a given L-shell is at lower

altitudes of the atmosphere in the American sector. At ionospheric heights, Earth's field deviates significantly from the centered dipole, compared to eccentric dipole [14]. Therefore, eccentric dipole coordinate systems are mainly used in ionospheric study for accuracy.

The International Geomagnetic Reference Field (IGRF) is one of the most accurate global models of the Earth's internally generated magnetic field [10]. IGRF is the negative gradient of a magnetic scalar potential V_B:

$$\vec{B}(r,\theta,\phi,t) = -\vec{\nabla}V_B(r,\theta,\phi,t) \tag{2.11}$$

$$V_B(r,\theta,\phi,t) = a\sum_{\ell=1}^{N}\sum_{m=0}^{\ell}\left(\frac{a}{r}\right)^{\ell+1}\left(g_\ell^m(t)\cos m\phi + h_\ell^m(t)\sin m\phi\right)P_\ell^m(\cos\theta) \tag{2.12}$$

where r represents radial distance from the center of the Earth, $a = 6371.2$ km being the geomagnetic conventional Earth's mean reference spherical radius, θ denoting geocentric co-latitude. V_B is represented with a spherical harmonics basis including harmonic terms in geocentric longitude ϕ and Legendre polynomial P_ℓ^m. Three output components of Earth's magnetic field are provided in a geographic spherical coordinate system, B_r, B_θ, B_ϕ (geographic radial, colatitude, and longitude directions), given an input geographic latitude, longitude, altitude, and time.

IGRF is a multipole expansion of the potential, the largest term of which is the dipole [10]. The terms with $l = 1$ produce a centered dipole model. Coefficients g_ℓ^m, h_ℓ^m are updated and published approximately every five years due to the time variation of Earth's magnetic field, notably in the drift of the poles. The version of the IGRF model and coefficients used in this work are those of the 12th generation (IGRF-12) [10].

2.3 SAMI3

SAMI3 (Sami3 is Also a Model of the Ionosphere) [15] is a three-dimensional global model based on two dimensional model SAMI2 [16]. This model treats the

plasma dynamics and chemical evolution of 7 ion species $H^+, He^+, N^+, {N_2}^+, NO^+, {O_2}^+$, and O^+. SAMI3 models the plasma along a magnetic flux tube from hemisphere to hemisphere. SAMI3 produces electric potential as output as well as $\vec{E} \times \vec{B}$ drifts.

The model solves the dynamics of the ionosphere on an eccentric dipole system known as the Apex coordinate system, to achieve better accuracy with respect to the magnetic field than the centered dipole coordinate. The native SAMI3 output will be on an Apex coordinate system. This coordinate system will be discussed in more detail in Chapter 4.

2.4 Lagrangian coherent structures

Coherent structures in a fluid are features that persist over some period of space and time that are not part of the mean flow [17]. An example is shown in Figure 2.3, with the Great Red Spot of Jupiter, which is an anti-cyclonic storm larger than Earth that has lasted for over a hundred years.

Defining coherent structures such as a vortex in an Eulerian frame is observer-dependent. If the observer is also rotating, a vortex apparent in one frame might not seem to exist in another Eulerian frame. The Lagrangian reference frame moves with the fluid element. Identifying coherent structures in a Lagrangian frame has been found to be observer-independent, or objective [5].

As an example, consider a flow of two counter-rotating vortices that alternately expand and contract. At any instant t_0, there is an invisible dividing line between the vortices. Fluid elements starting on one side of the dividing line will flow in one vortex, and fluid elements on the other side of the dividing line will circulate to the other vortex. All observers will see the same behavior of the fluid elements. The Lagrangian coherent structure (LCS) is the dividing line (or surface in 3D) that separates the two regions exhibiting different fluid behavior. For the time-varying

Figure 2.3. Example of coherent structures in the atmosphere of Jupiter. This full-disc image of Jupiter was taken on 21 April 2014 with Hubble's Wide Field Camera 3 (WFC3). Image credit: Wikimedia [18]

double-gyre, the yellow ridge shown in Figure 2.4 illustrates the LCS.

As time passes, points A, B, C which are originally equally spaced from each other at A_0, B_0, C_0 travel from the top to the bottom of the plot, ending at A_f, B_f, C_f. In Figure 2.4a, A_f, B_f end at the lower right but C_f ends at the lower left. The yellow LCS ridge separates the points in the initial flow that will have significantly different tracer trajectories. The fact that B_0, C_0 end up at opposite regions of the domain is indicated by the fact that the LCS ridge separates B_0, C_0 at time t_0. The LCS describes points at time t_0 that will separate apart; no particles will mix across the yellow coherent structure. The LCS itself moves with the flow over time as well; this is why the LCS at t_0 appears to be crossed by the particles at various times $t > t_0$ as they start from A_0, B_0, C_0 traveling to A_f, B_f, C_f.

The initial time t_0 considered in a time-varying flow will affect the LCS position. In Figure 2.4b, although particles A, B, C have same initial positions as in Figure 2.4a, for $t_0 = 0.96$ s only particle A will arrive in the lower right of the domain, as the coherent structure was positioned between A_0, B_0 at the beginning. In other words, the LCS ridge can be used to predict or constrain the behavior of initial particles over time.

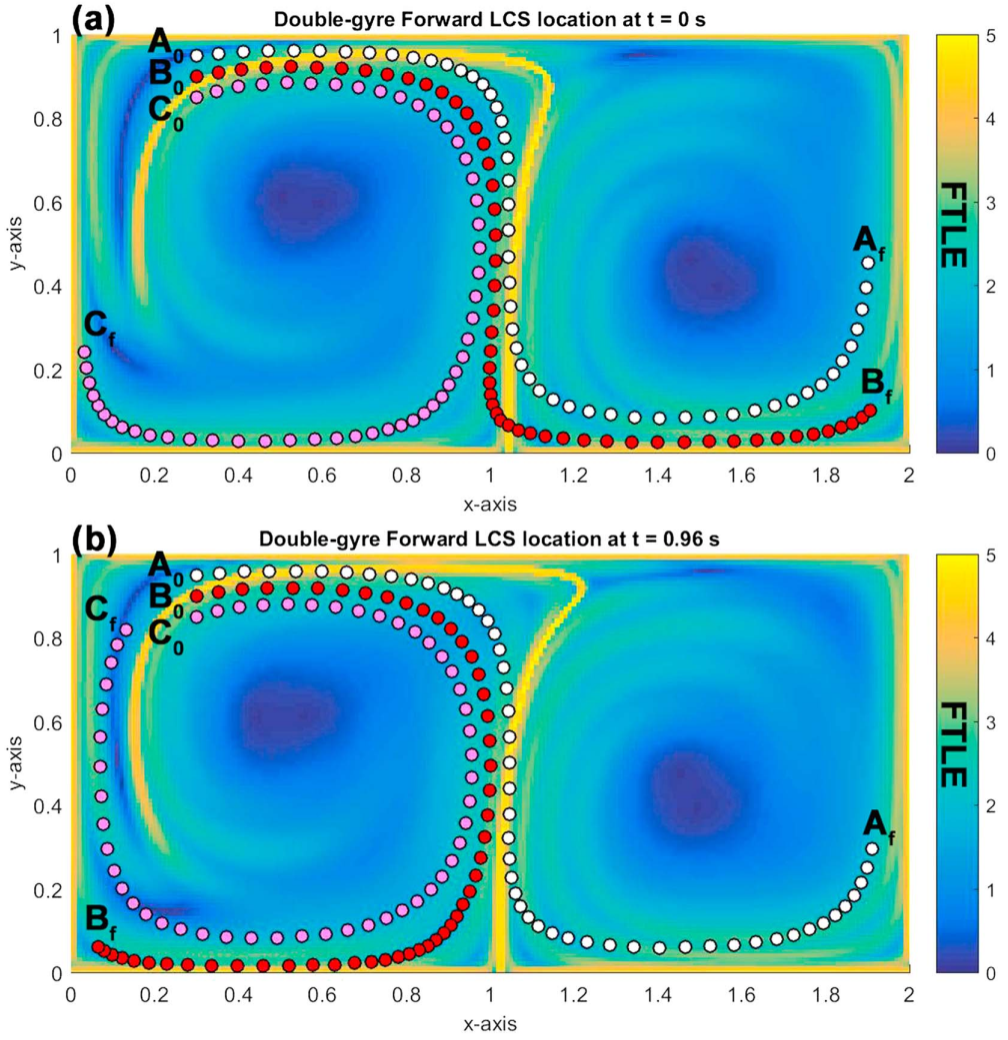

Figure A1. Finite-time Lyapunov exponent (FTLE) map for time-varying double-gyre field for (a) $t_0 = 0$ s. (b) $t_0 = 0.96$ s with the integration time $\tau = 1$ s. The color scale in each map represents the FTLE value ranging from 0 to 5. The three traers' initial and final positions are labeled as A_0 and A_f for white, B_0 and B_f for red, and C_0 and C_f for magenta.

Figure 2.4. Double-gyre LCSs (yellow) for two different initial times. Reprinted from [8].

The most commonly used method for finding LCSs is to compute the finite-time Lyapunov exponent (FTLE) [4]. A flow map $\vec{F}$ is a mapping of fluid elements starting at position $\vec{x}_0$ at time t_0 in a domain to a position at time t_f after flowing in velocity field $\dot{\vec{x}}$ which may be time-varying.

$$\dot{\vec{x}} = \vec{v}(\vec{x}, t) \tag{2.13}$$

$$\vec{F}_{t_0}^{t_f}(\vec{x}_0) = \vec{x}(t_f; \vec{x}_0, t_0) \tag{2.14}$$

$$= \vec{x}_0 + \int_{t_0}^{t_f} \vec{v}(\vec{x}, t)dt \tag{2.15}$$

The flow map can be computed by integrating each particle according to the velocity along its trajectory. The linearization of the flow map describes how perturbations in initial position affect the final position. The linearization is a matrix of first derivatives of components of $\vec{F}$ with respect to each coordinate component x_i:

$$\mathbf{J} = \begin{bmatrix} \frac{\partial F_1}{\partial x_1} & \frac{\partial F_1}{\partial x_2} \\ \\ \frac{\partial F_2}{\partial x_1} & \frac{\partial F_2}{\partial x_2} \end{bmatrix} \tag{2.16}$$

The finite-time Lyapunov exponent σ is the normalized largest eigenvalue, λ_{max}, of $\mathbf{J}^T\mathbf{J}$:

$$\sigma(\mathbf{J}) = \frac{1}{|\tau|} \log\left(\sqrt{\lambda_{max}(\mathbf{J}^T\mathbf{J})}\right) \tag{2.17}$$

where τ is duration $t_f - t_0$. This largest eigenvalue describes the maximum amount of stretching at a given initial point. The Jacobian can be computed for each initial point in the domain. The locus of points with the maximum FTLE over the domain defines regions of the initial domain that will undergo the most stretching. The set of points with locally maximum FTLE is defined as the Lagrangian coherent structure.

Returning to Figure 2.4, the color of each pixel in the field indicates the FTLE value at that initial point. The LCS is the set of points indicated by the yellow ridge,

whose FTLE value is locally maximum at about a value of 5 s^{-1}. The set of points comprising the the LCS in Figure 2.4a differs from the set of points of the LCS in Figure 2.4b. This means that the LCS depends on the initial time t_0 because the flow mapping $\vec{F}$ differs with initial time in a time-varying flow. It also differs with integration time τ (not shown).

2.5 ITALCS

Over the past several years, the ionosphere-thermosphere algorithm for LCSs (ITALCS) has been developed to compute the FTLE map for determining LCSs on a spherical surface. It uses generalized coordinates of latitude λ and longitude ϕ for coordinates x_1, x_2 on a regularly spaced grid. ITALCS implements the flow map by integration according to Eq. (2.15) ITALCS additionally wraps particles on a latitude-longitude grid around the globe and over the poles such that the domain remains closed. The equations describing this wrapping of coordinates are in [8]. Then the FTLE is computed as the normalized maximum singular value of **J** in Eq. (2.16) at each point, and can be plotted on a map of the globe.

If velocity fields are provided as linear ground speeds east v_e and north v_n, they must be converted to angular rates $\dot{\lambda}, \dot{\phi}$ to correspond to the λ, ϕ coordinates for integration as:

$$\dot{\phi} = \frac{v_e}{r \cos \lambda} \tag{2.18}$$

$$\dot{\lambda} = \frac{v_n}{r} \tag{2.19}$$

In this work $r = R_E + h$ where the mean radius of Earth is $R_E = 6371.2$ km and h is the altitude above the surface of Earth. Note that $\dot{\phi}$ becomes undefined at the poles.

Previous researchers have used ITALCS with geographic latitude and longitude to show that ionospheric LCSs are located at high latitudes and, according to an empirical model, are horseshoe-shaped [8]. Using data-derived electric potential on a

geomagnetic latitude and longitude grid, the shape was found to be more structured possibly as a "W" around the pole [11]. The closed side was oriented toward the local daytime longitude and the opening on the nightside. In both cases, polar cap patches were confined and separated in their movement from other regions of high plasma density.

CHAPTER 3

VECTOR ROTATION FROM LOCAL MAGNETIC COORDINATES TO GEOGRAPHIC COORDINATES

When using ITALCS, the velocity field $\vec{v}$ must be specified in the same coordinate components as the spatial gridpoints, in order to complete the integration of the particle velocity over its trajectory according to Eq. (2.15).

For this study, collaborators provided $\vec{E} \times \vec{B}$ drifts output from SAMI3 on a regular geographic grid of longitude ϕ and latitude λ. The velocity components provided are "u_r component of ExB drift velocity (radial)"; and "u_z component of ExB drift velocity (magnetic zonal)," each in units of cm/s.

Given the descriptions, I considered the component directions as a curvilinear coordinate system with one unit vector oriented along the local magnetic field line. These "local magnetic coordinates" (Section 3.2 of [14]) are commonly used in ionospheric dynamics. In this magnetic field coordinate system, seen in Figure 3.1, $\hat{u}_h$ is a unit vector that points along the field line, $\hat{u}_z$ perpendicular to the field line eastward (magnetic zonal), and $\hat{u}_r$ perpendicular to the $\vec{B}$ field, in the magnetic-meridional plane. Since the vector elements are ion drift velocities, from the $\vec{E} \times \vec{B}$ cross product, the u_h vector component of the drift, which is along the B field, is zero.

3.1 Vector rotations

For the goal of obtaining LCSs by inputting SAMI3 drifts to ITALCS, conversion to geographic coordinates is necessary. The first method used for transforming from local magnetic field coordinates to geographic coordinates is shown in Figure 3.2.

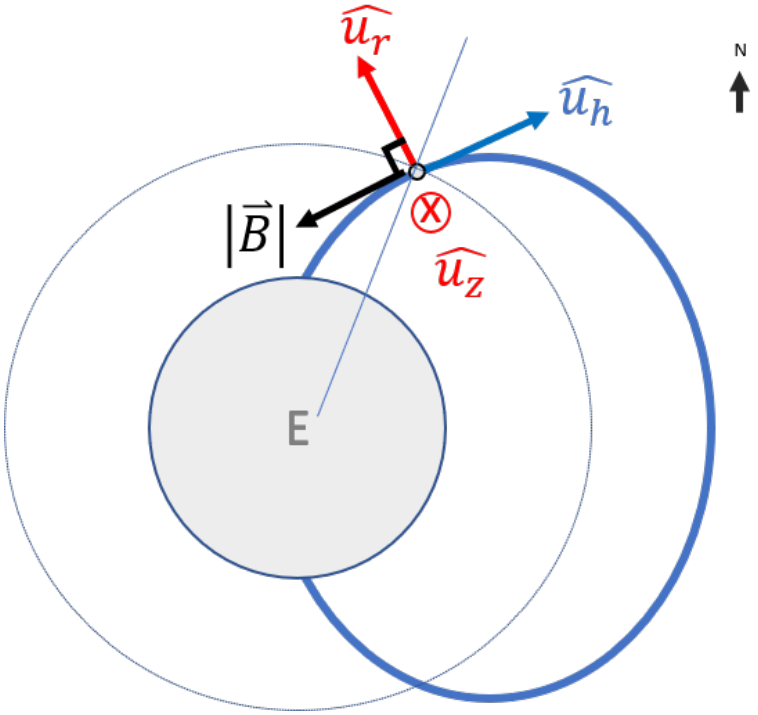

Figure 3.1. Local magnetic field coordinates. Unit vector $\hat{u}_h$ points along the field line, $\hat{u}_z$ is perpendicular to the field line eastward (magnetic zonal), and u_r is perpendicular to the $\vec{B}$ field, in the magnetic meridional plane. At the magnetic equator $\hat{u}_r$ points radially outward and $\hat{u}_h$ is horizontal. Since the vector elements are ion drift velocities, from the $\vec{E} \times \vec{B}$ cross product, the $\hat{u}_h$ vector component of the drift, which is along the B field, is zero.

The first step is to rotate the velocity vector from local magnetic coordinates to a magnetic East-North-Up (ENU) system. This rotation can be done using the inclination angle I. The inclination angle is the angle between the magnetic field line and the local horizontal vector in the plane containing the magnetic field line as shown in Figure 3.3. We also call this angle the dip angle because the magnetic field dips down when it gets closer to the north pole. The inclination angle is defined positive downward, so is positive in the northern hemisphere and negative in the southern hemisphere.

When we consider converting local magnetic coordinates to magnetic ENU (see Figure 3.3), at the magnetic equator, the magnetic northward unit vector is horizontal

and magnetic ENU upward unit vector points radially away from the center of Earth. Based on this relation, inclination allows for a vector rotation between magnetic field and magnetic ENU coordinates as:

$$\begin{bmatrix} m_E \\ m_N \\ m_U \end{bmatrix} = \begin{bmatrix} 1 & 0 & 0 \\ 0 & \sin I & -\cos I \\ 0 & \cos I & \sin I \end{bmatrix} \begin{bmatrix} u_z \\ u_r \\ u_h \end{bmatrix} \tag{3.1}$$

After the first rotation, an additional rotation is required to transform to geographic vectors. To convert magnetic ENU to geographic ENU vector elements, declination is used. Declination angle is the angle between the horizontal component of the magnetic field and the local geographic north direction. Declination is positive when magnetic north points eastward of geographic north as shown in Figure 3.4. The rotation axis will be the upward unit vector $\hat{M}_u = \hat{G}_u$ shown in Figure 3.5. Given the declination angle D, geographic ENU components are found from the following matrix equation:

$$\begin{bmatrix} g_E \\ g_N \\ g_U \end{bmatrix} = \begin{bmatrix} \cos D & \sin D & 0 \\ -\sin D & \cos D & 0 \\ 0 & 0 & 1 \end{bmatrix} \begin{bmatrix} m_E \\ m_N \\ m_U \end{bmatrix} \tag{3.2}$$

The inclination and declination angle can be determined from the International Geomagnetic Reference Field (IGRF). For a given location, IGRF produces the three components of the magnetic field in geographic spherical coordinates as:

$$\vec{B} = B_\phi \hat{G}_E - B_\theta \hat{G}_N + B_r \hat{G}_U \tag{3.3}$$

with B_r the vertical component, B_θ the geographic southward component, and B_ϕ the geographic eastward component. Based on the magnetic field vector direction as

shown in Figure 3.3 and Figure 3.7, declination D and inclination I can be found as:

$$D = \tan^{-1}\left(\frac{B_\phi}{-B_\theta}\right) \tag{3.4}$$

$$I = \tan^{-1}\left(\frac{B_r}{\sqrt{B_\theta^2 + B_\phi^2}}\right) \tag{3.5}$$

After the coordinate rotation, the SAMI3 ion velocity data are converted to angular rates according to Eqs. (2.18)-(2.19) and then are ready to be input to ITALCS.

3.2 Result

The FTLE map over the north pole for $t_0 = 1$ January 2014 00:00 UT and an integration time of $\tau = 3$ hours is shown in Figure 3.8. The FTLE values converge to the pole, which looks very different from the horseshoe shape we expect to see based on the literature. While some of the inaccuracy may be due to the singularity of angular speed at the pole, in the end I determined that the coordinate system in which SAMI3 drifts were provided was not in fact the local magnetic coordinate system. The true SAMI3 coordinate system will be discussed in the next chapter.

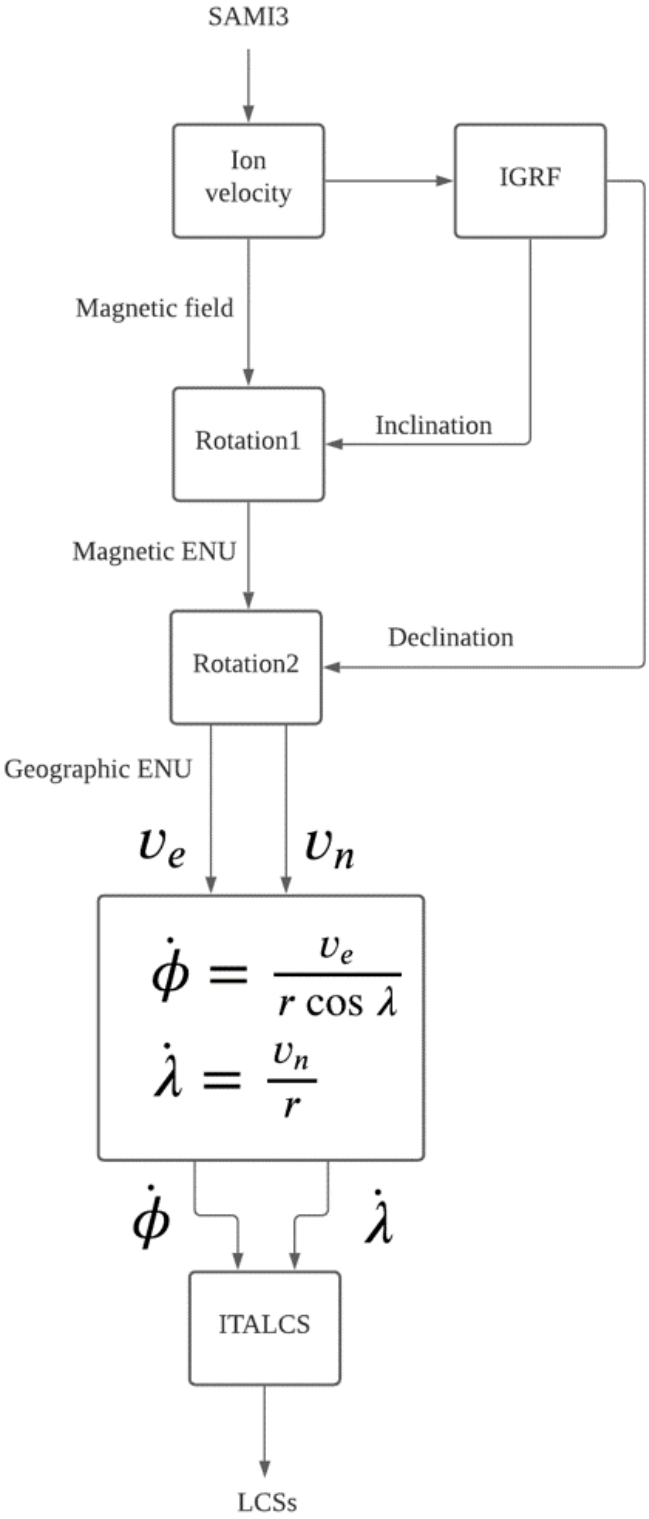

Figure 3.2. Overview of method 1 processing. When ion velocity is given in magnetic field coordinates, two vector rotations and speed conversion will be required before input to ITALCS.

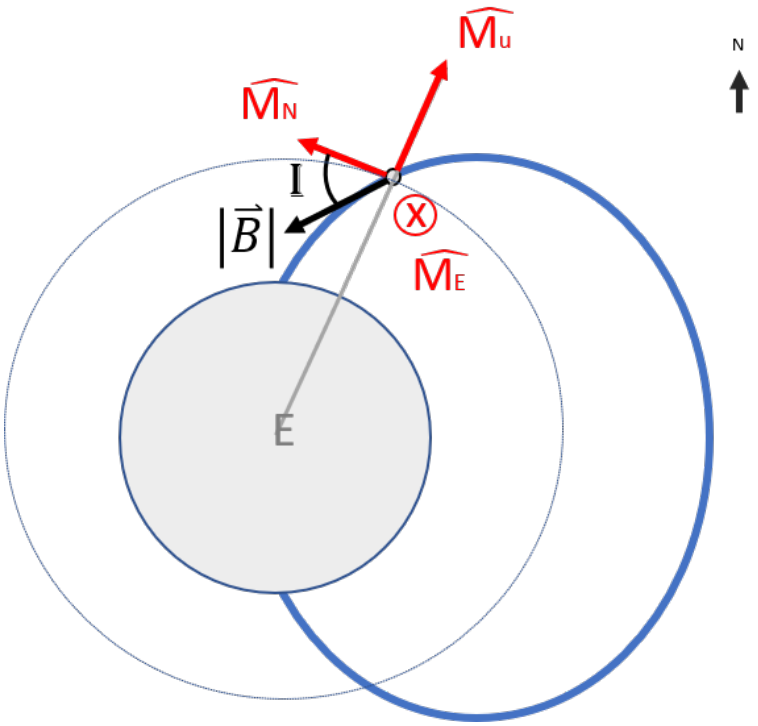

Figure 3.3. Magnetic ENU. Magnetic eastward unit vector, $\hat{M}_E$, is perpendicular to the field line eastward. Magnetic northward unit vector, $\hat{M}_N$, is horizontal and a vector in the plane of the field line. Magnetic ENU upward unit vector, $\hat{M}_U$, points radially away from the center of Earth.

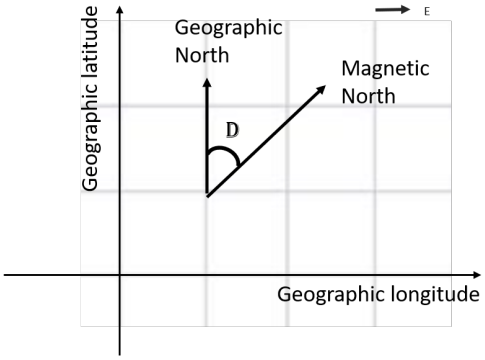

Figure 3.4. Definition of declination. Declination is positive when magnetic north points eastward of geographic north.

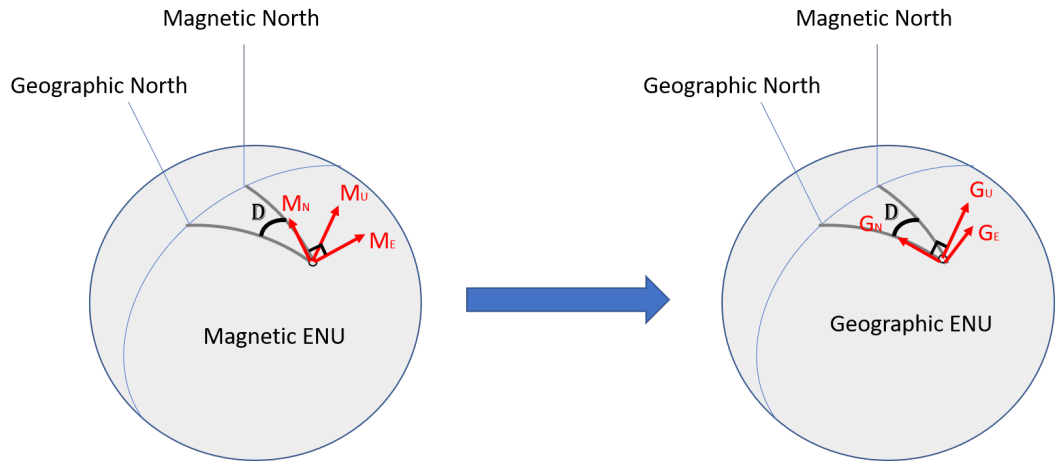

Figure 3.5. Declination angle and coordinate rotation from magnetic ENU to geographic ENU. Upward unit vectors $\hat{M}_U$ and $\hat{G}_U$ point in the same direction. Magnetic north unit vector $\hat{M}_N$ is aligned with the line from the point toward the North Magnetic Pole. Similarly, $\hat{G}_N$ is points toward the North Geographic Pole. $\hat{M}_E$ is perpendicular to the field line eastward. $\hat{G}_E$ is perpendicular to the vectors, $\hat{G}_U$ and $\hat{G}_N$, eastward.

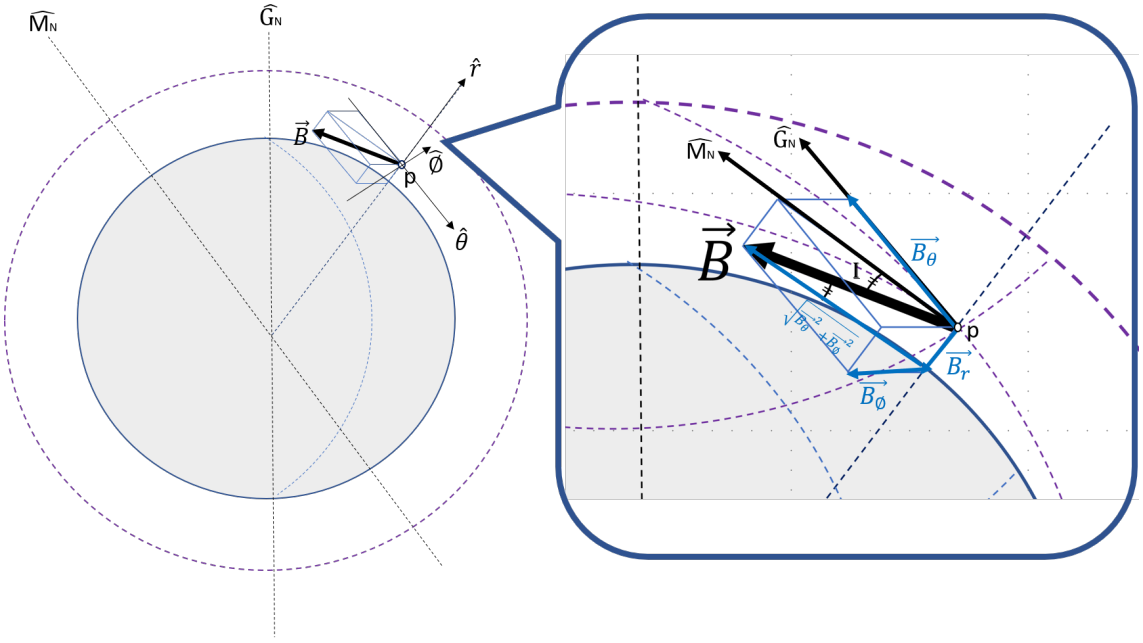

Figure 3.6. Obtaining inclination angle from IGRF. $\hat{r}$, $\hat{\phi}$, and $\hat{\theta}$ are positive unit axes in IGRF. $\vec{B}_r$, $\vec{B}_\theta$, and $\vec{B}_\phi$ are decomposed elements of magnetic field, $\vec{B}$.

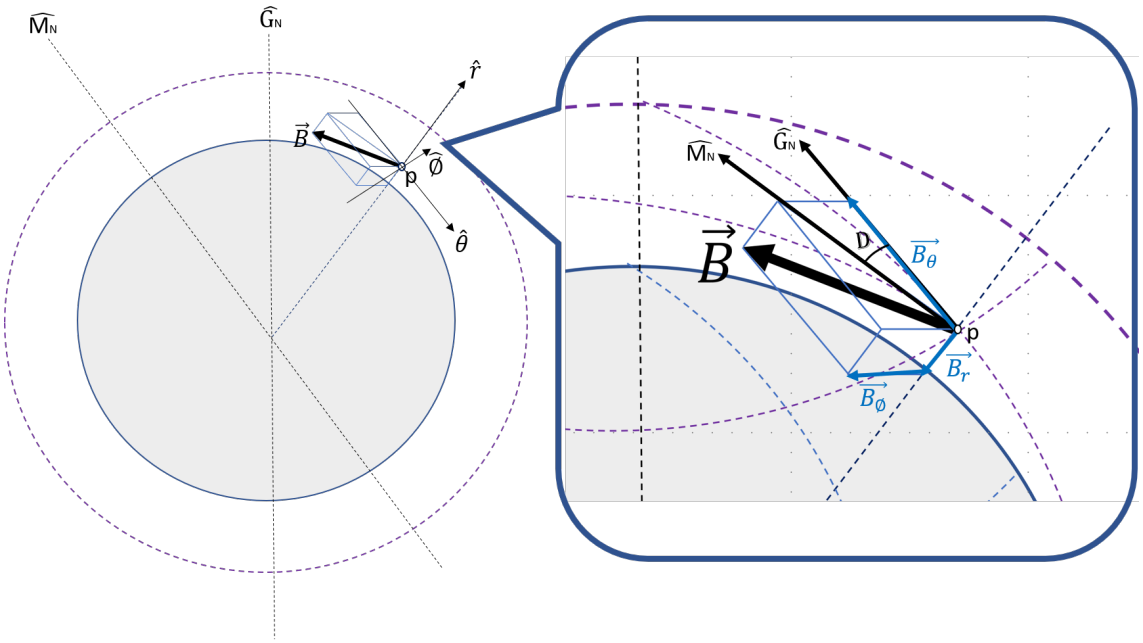

Figure 3.7. Obtaining declination angle from IGRF. $\hat{r}$, $\hat{\phi}$, and $\hat{\theta}$ are positive unit axes in IGRF. $\vec{B_r}$, $\vec{B_\theta}$, and $\vec{B_\phi}$ are the decomposed horizontal elements of magnetic field, $\vec{B}$.

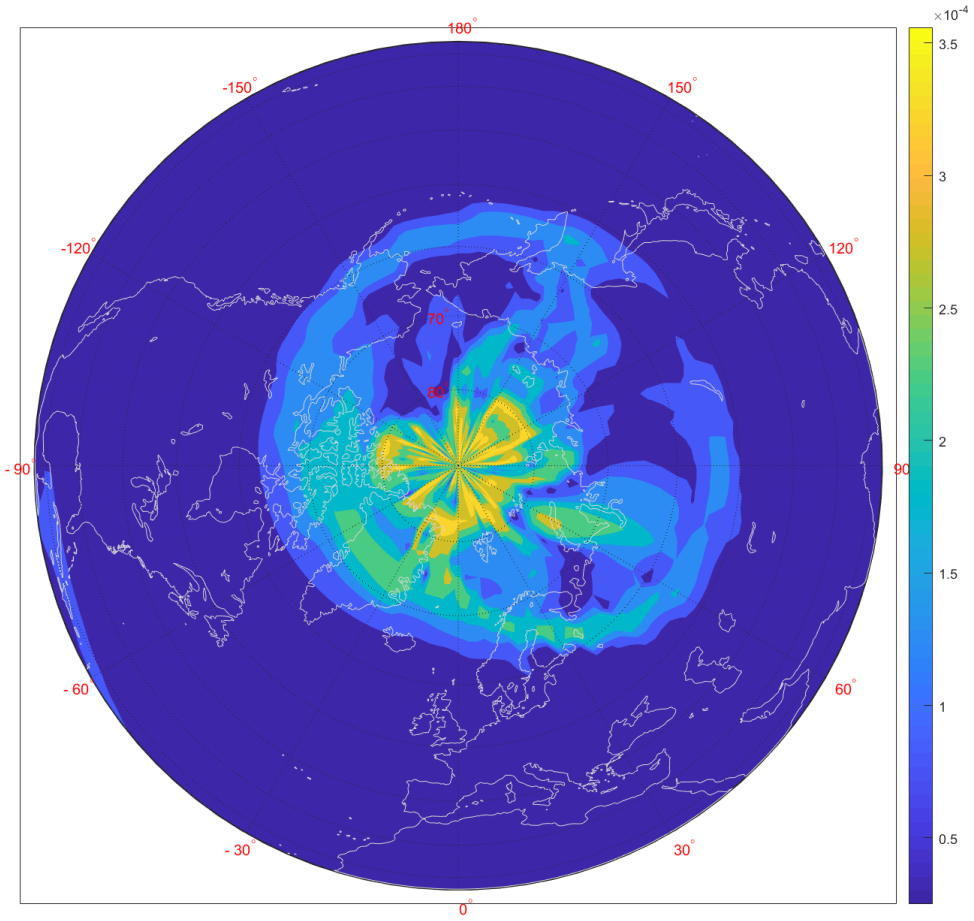

Figure 3.8. Finite-time Lyapunov exponent map of SAMI3 plasma drifts at 300 km over the northern hemisphere for initial time t_0 =1 January 2014 00:00 UT, integration time $\tau = 3$ hours. The color scale represents the FTLE values ranging from 0 to 3.5×10^{-4} s^{-1}.

CHAPTER 4

TRANSFORMATION OF NON-ORTHOGONAL VECTORS

After clarifying with the model output providers that the coordinate system of the SAMI3 outputs is not the local magnetic field system, a new method for transformation was required. SAMI3 runs on the Apex coordinate grid. Apex coordinates are a curvilinear system that is non-orthogonal [14].

Orthogonal coordinate systems, such as the geographical coordinate system $\hat{G}_E, \hat{G}_N, \hat{G}_U$ introduced in the previous chapter, are commonly used in mechanics. They are convenient because matrix rotations allow us to convert from one orthogonal system to another. However, non-orthogonal vectors require different steps for a coordinate transformation. In this chapter, I review the Apex coordinate system and provide a method of converting Apex coordinate vector components into geographic vector components.

4.1 Apex coordinates

While dipole coordinates or spherical coordinates are simpler to use for ionospheric studies, coordinates with non-dipolar components are considered more accurate because they account for multi-pole magnetic field components and Earth oblateness [19]. Apex latitude and longitude coordinates are often used in ionospheric electrodynamic calculations. This is because the strong influence of the geomagnetic field on charged-particle motion in the ionosphere prevents the charged particles from crossing the field lines. Therefore, modeling ionospheric behavior based on magnetic field is more sensible [14].

The Apex coordinate system is based on the concept of a magnetic shell,

analogous to the L-shell. For an oblate Earth the apex of the field line is defined to be the point on the magnetic line (obtained using IGRF) that is a maximum height above the ellipsoid [20]. The apex shell consists of all the magnetic field lines whose apexes are at a given height h_A above the surface of the Earth. Apex latitude specifies a particular apex shell. Apex longitude specifies a particular field line in the shell, and its height above the Earth, which specifies two points on the magnetic field line in the northern and southern hemispheres.

Apex latitude λ_A is:

$$\lambda_A = \pm \cos^{-1} \sqrt{\frac{R_E}{R_E + h_A}} \tag{4.1}$$

where R_E is the equatorial radius of the ellipsoid of Earth, and h_A is apex height, the height of the apex of the field line above the geoid. Any point along a single field line will have the same λ_A. In this way the latitude coordinate can be used analogously to the "L" parameter to refer to a quantity that is constant for a given field line.

Apex longitude ϕ_A is:

$$\phi_A = \sin^{-1} \left(\frac{\cos\lambda \sin(\phi - \phi_0)}{\cos\lambda_D} \right) \tag{4.2}$$

where λ_D, the dipole latitude, is given by

$$\lambda_D = \sin^{-1} \left(\sin\lambda \sin\lambda_0 + \cos\lambda \cos\lambda_0 \cos(\phi - \phi_0) \right) \tag{4.3}$$

Here λ and ϕ are the geographic latitude and longitude, respectively. The geographic latitude and longitude of the north pole of the earth-centered dipole are λ_0 and ϕ_0, respectively [20].

Apex coordinates have the same form as general curvilinear coordinates, as illustrated in Figure 4.1. Given that the velocity components mentioned at the beginning of Chapter 3 provided by SAMI3 are "u_r component of ExB drift velocity

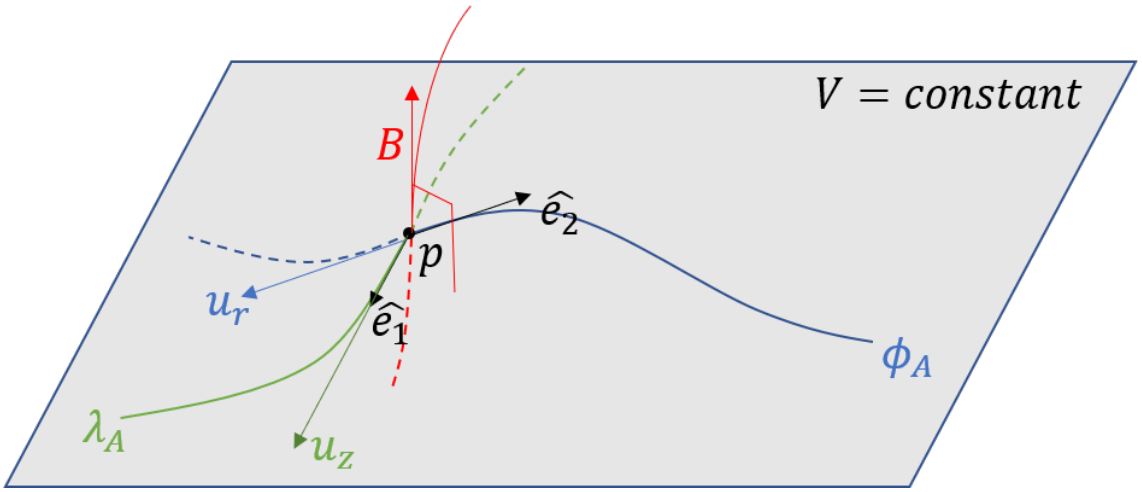

Figure 4.1. Illustration of general curvilinear coordinates as Apex coordinate components. Constant contour λ_A, ϕ_A are on a surface of constant magnetic potential V. At point p the $\hat{e_1}$ vector is tangent to coordinate contour λ_A, $\hat{e_2}$ vector is tangent to coordinate contour ϕ_A. Ion velocity components u_z and u_r align with $\hat{e_1}$ and $\hat{e_2}$, respectively.

(radial)"; and "u_z component of ExB drift velocity (magnetic zonal)," each in units of cm/s.

Redefining the velocity components in terms of the Apex coordinate system, the unit vector $\hat{e_1}$ is tangent to coordinate contour λ_A, and points eastward tangent to the Apex latitude line. The ion velocity component aligned this vector is u_z. The $\hat{e_2}$ vector is tangent to coordinate contour ϕ_A and points equatorward. The ion velocity component aligned with this vector is u_r, positive in $-\hat{e_2}$ direction. In other words, SAMI3 drifts are expressed as

$$\vec{v}_{ExB} = u_z\hat{e_1} - u_r\hat{e_2} \tag{4.4}$$

Finally, $\hat{e_3}$ is aligned with the IGRF magnetic field, meaning $\hat{e_3} = -\hat{u}_h$, with $\hat{u}_h$ as defined in the previous chapter in Figure 3.1.

4.2 Concept for transforming velocity from Apex coordinate directions

Equations 4.1 and 4.2 provide scalar coordinate conversions for latitude and

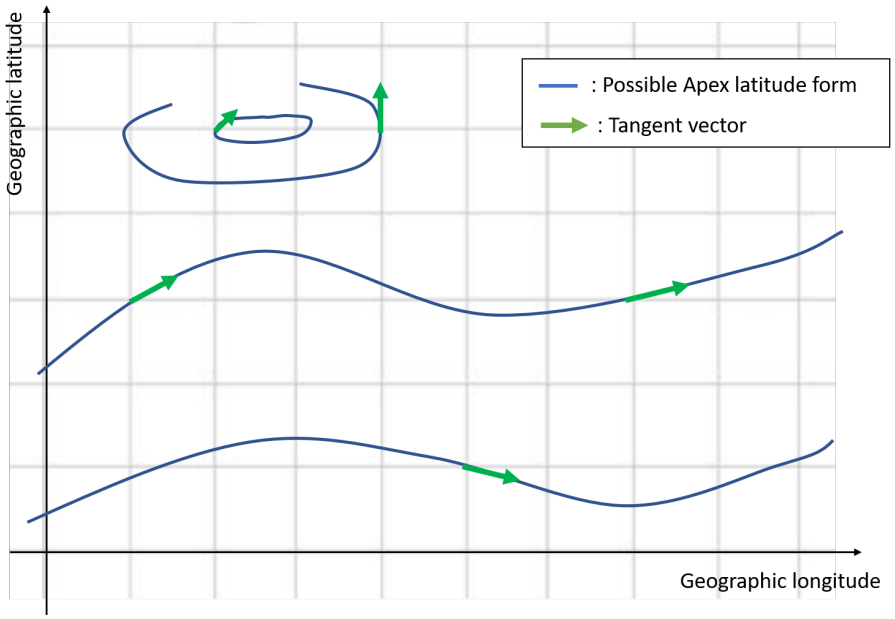

(a) Apex latitude tangent vectors. The blue lines are constant Apex latitude contours. Green arrows pointing eastward show tangent vectors at specific grid points, corresponding to $\hat{e}_1$ mentioned in Figure 4.1.

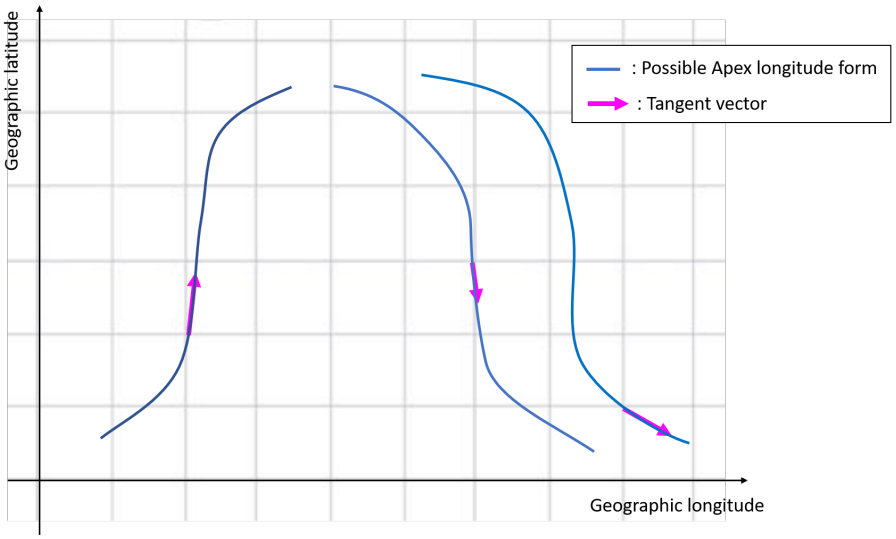

(b) Apex longitude tangent vectors. The blue lines are constant Apex longitude contours. Magenta arrows pointing equatorward show tangent vectors at specific grid points corresponding to $\hat{e}_2$ mentioned in Figure 4.1.

Figure 4.2. Illustration of Apex latitude and longitude tangent vectors. The gray grid represents geographic coordinates.

longitude, but do not specify a vector transformation. Therefore, I present a way to derive the apex coordinate unit vector directions. The concept is illustrated here, with numerical steps given in Section 4.3.

Figure 4.2(a) illustrates individual lines of Apex latitude on a geographical latitude/longitude map. Each curve represents one specific Apex latitude value. As mentioned in the discussion of Figure 4.1, tangent vectors on each line represent the unit axis at a given point. Therefore, a green tangent vector is the direction of one of the Apex unit vector directions, i.e., the zonal direction. Figure 4.2(b) shows curves of constant Apex longitude in blue. The magenta arrow is a tangent vector at each specific point. This tangent vector is also one unit vector in Apex magnetic coordinates at a given point. As we are considering $\vec{E} \times \vec{B}$ drift, each velocity will have components in the eastward and equatorward directions. The third direction is parallel to $\vec{B}$ locally, and $\vec{E} \times \vec{B}$ will be orthogonal to it.

At a given gridpoint P, as shown in Figure 4.3(a), the tangent unit vectors can be found. The length of each arrow will be scaled by the plasma drift component given in the data along each direction (green and magenta arrows). Then at point P, as shown in Figure 4.3(b), each component will be decomposed into geographic zonal and meridional components (e.g., for u_z, the decomposition is drawn as $a_1\hat{G}_E - b_1\hat{G}_N$ in the Figure). The sum of the zonal $\hat{G}_E$ components will give the geographic zonal vector component speed (v_x on the Figure), and the sum of the meridional components will give the speed in the $\hat{G}_N$ direction. This yields the vector transformation of the velocity vector from Apex coordinate directions to geographic east and north directions.

4.3 Method for computing Apex coordinate tangent unit vector directions

In order to transform the velocity vector as described in the previous section,

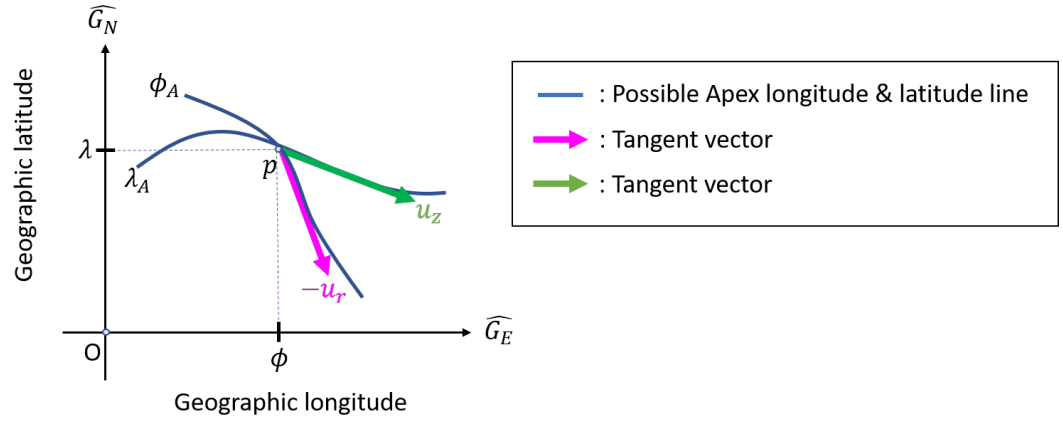

(a) At point P, tangent vectors on each Apex latitude and longitude will be green and magenta arrows. The length of each arrow will be given by the size of the plasma velocity component,u_r, u_z, provided along each axis.

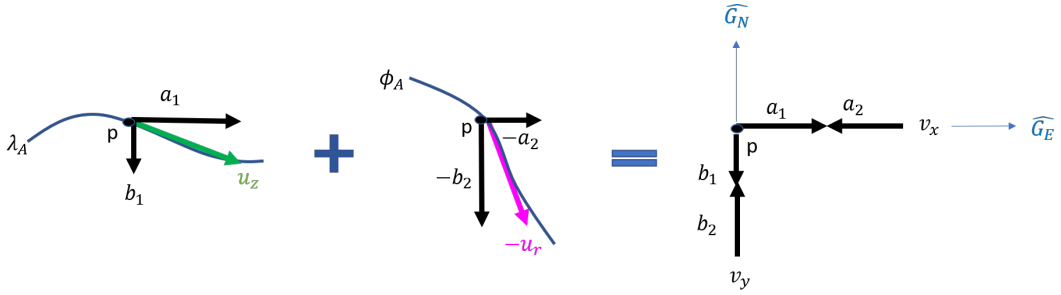

(b) At a specific point P, each Apex longitude and latitude vector can be decomposed into geographic zonal (east-west) and meridional (north-south) directions. After each decomposition, the vector elements on the same axis can be combined.

Figure 4.3. Vector decomposition of velocity components from $\hat{e}_1, \hat{e}_2$ non-orthogonal directions to $\hat{G}_E, \hat{G}_N$ directions.

I first find the tangent vectors $\hat{e}_1, \hat{e}_2$. The concept for the approach is shown in Figure 4.4. At a given point P whose geographic (λ, ϕ, h) are known, I compute its Apex coordinates λ_A. I then follow along the same λ_A holding it constant, to a neighborhing point P' a small longitudinal distance away. In the limit as the longitudinal separation approaches 0, the position vector of P' relative to P $\vec{r}^{P'} - \vec{r}^{P}$ becomes the tangent vector $\hat{e}_1$. Similarly, following from point P along the same Apex longitude ϕ_A line by holding it constant, I find a point P'' some small distance away. In the limit as

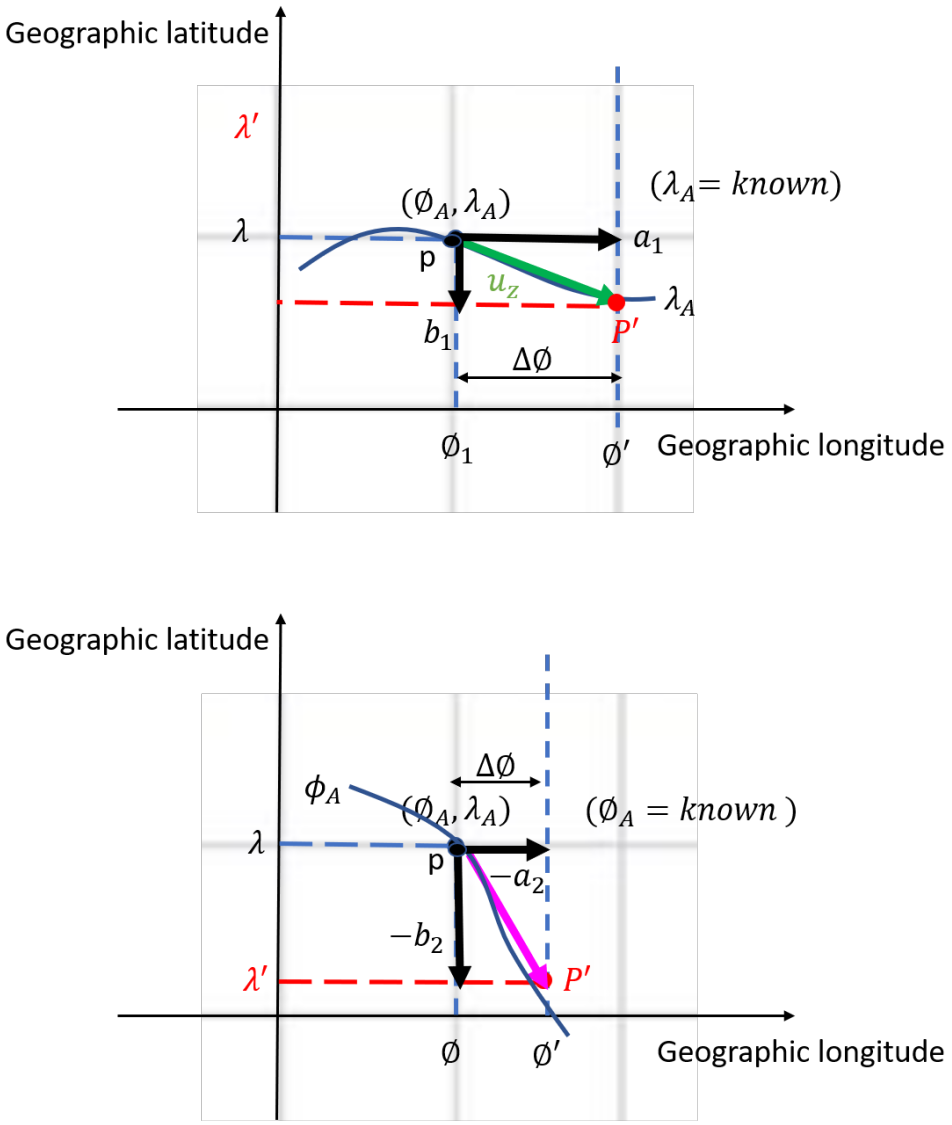

Figure 4.4. Grid point P and neighboring point P' have the same Apex value, Apex longitude, ϕ_A, or Apex latitude, λ_A. The coordinates ϕ, λ are the known geographic longitude and latitude, respectively, of P. For a given geographic longitude $\phi' = \phi + \Delta\phi$, and known apex value, ϕ_A or λ_A, the unknown λ, is found. Finding point P' enables calculation of the tangent vector at P for a small $\Delta\phi$.

P'' approaches P, the position vector difference $\vec{r}^{P''} - \vec{r}^{P}$ approaches $\hat{e}_2$.

The first step at a point P with geographic latitude λ, longitude ϕ and height h is to compute its Apex latitude and longitude. The Apex latitude requires an estimate of Apex height h_A. In this work I approximate h_A in Equation 4.1 using the

L-shell:

$$h_A \;=\; R_E(L-1) = \left(\frac{R_E + h}{\cos^2 \lambda_m} - R_E\right) \tag{4.5}$$

This equation is based on a dipole magnetic field, which is simpler than the true Apex coordinate system height found by tracing the IGRF multipole field lines. The L-shell Equation 2.10 is a function of geomagnetic latitude λ_m. Therefore, IGRF is used to get geomagnetic latitude λ_m from the geographic longitude ϕ, latitude λ, and height h of point P. After finding h_A from the L-shell equation, Equation 4.1 gives the apex latitude of point P. The choice to use L-shell is for simplicity, letting us take the gridpoint's geographic λ, ϕ, h and plug them directly into Eqs. (4.1)-(4.2).

In Eq. (4.3) the values for the north pole of the Earth-centered dipole are assumed to be $\lambda_0 = 79°$, $\phi_0 = -69°$, respectively, found from [20]. Note that the location of the magnetic pole changes over time, so this also may introduce some inaccuracy.

The full process beginning with $\vec{v}_{ExB}$ specified as in Equation (4.4) and resulting in $\vec{v}_{ExB} = v_x \hat{G}_E + v_y \hat{G}_N$ is detailed in the flowchart in Figure 4.5. At a point P having geographic latitude, longitude, height, and time (λ, ϕ, h, t) the plasma drift velocity is given in Apex coordinate directions $\hat{e}_1, -\hat{e}_2$. Inputting the latitude, longitude, and height into IGRF subroutine geodip, the magnetic latitude λ_m is found for point P. This is used to calculate the L-shell according to Eq. (2.10) and then the apex height in Eq. (4.5). Thus the Apex longitude and latitude ϕ_A, λ_A for point P can be mapped independently from its geographic coordinates ϕ, λ, h using Eqs. (4.1)-(4.2).

To find the geographic latitude λ' at a nearby point P' along the same apex latitude line, I use known geographic longitude $\phi' = \phi + \Delta\phi$ because same λ_A has constant h_A in Eq. (4.1) and constant magnetic latitude λ_m in Eq. (4.5).

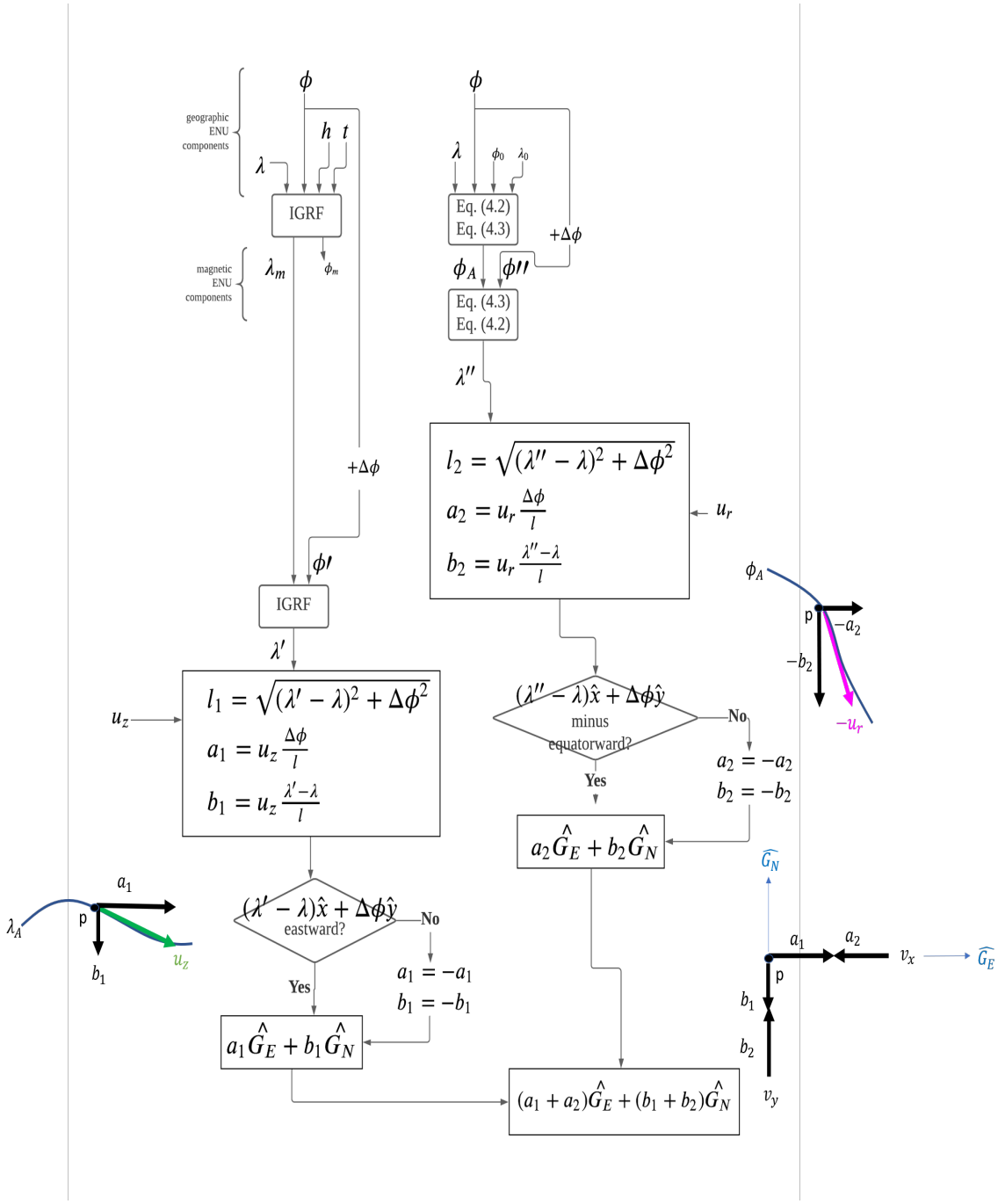

Figure 4.5. Overall process of Apex coordinate vectors projection. To obtain tangent vectors aligned with each Apex latitude and longitude, first, we have to find Apex latitude and Apex longitude at each geographic point. After that each tangent vectors are projected to geographic longitude and latitude. The two geographic vectors from each Apex latitude and Apex longitude are combined at the end.

When λ' is found, in the limit as $\Delta\phi$ is chosen small enough, the spherical surface on which P and P' lie is well-approximated as Euclidean plane on which the relative position vector of P' relative to P lies. The line between P and P' approaches the tangent to the Apex latitude line at point P:

$$\vec{e}_1 = \lim_{\Delta\phi\to 0} \vec{r}^{P'} - \vec{r}^{P} \approx R_E(\lambda' - \lambda)\hat{G}_N + R_E(\phi' - \phi)\hat{G}_E \tag{4.6}$$

The tangent vector to Apex latitude at each grid point is chosen to point positive eastward to match the description of the sign convention of the velocity data provided (Figure 4.2(a)).

Finding the tangent vector to the Apex longitude line has a similar process. From Figure 4.4, for a point P whose geographic longitude ϕ and latitude λ are known, Eqs. (4.2)-(4.3) give the Apex longitude, ϕ_A. I find the unknown geographic latitude λ'' from known $\phi'' = \phi + \Delta\phi$ and ϕ_A by applying these two known values in Eqs. (4.2)-(4.3) and solving for λ''. As $\Delta\phi$ becomes infinitesimally small, the line between P and P'' can be considered close enough to tangent to the apex longitude line at point P.

$$\vec{e}_2 = \lim_{\Delta\phi\to 0} \vec{r}^{P''} - \vec{r}^{P} \approx R_E(\lambda'' - \lambda)\hat{G}_N + R_E(\phi'' - \phi)\hat{G}_E \tag{4.7}$$

Tangent vectors to Apex longitude lines are defined to be positive equatorward (Figure 4.2(b)) [14]. Note that SAMI3 data is positive in the poleward direction.

From the velocity data given, the magnitude of drift velocity components aligned with each $\vec{e_i}$ is known. Therefore, zonal direction ion velocity u_z will decom-

posed into geographical coordinate components, a_1 and b_1, as:

$$l_1 = \sqrt{(\lambda' - \lambda)^2 + \Delta\phi^2} \tag{4.8}$$

$$\hat{e}_1 = \frac{1}{R_E l_1}\vec{e}_1 \tag{4.9}$$

$$a_1 = (\vec{v}_{ExB} \cdot \hat{e}_1)\hat{e}_1 \cdot \hat{G}_E = u_z \frac{\Delta\phi}{l_1} \tag{4.10}$$

$$b_1 = (\vec{v}_{ExB} \cdot \hat{e}_1)\hat{e}_1 \cdot \hat{G}_N = u_z \frac{\lambda' - \lambda}{l_1} \tag{4.11}$$

where l_1 is the norm of the relative position vector $\vec{e}_1$ normalized by R_E.

Also, ion velocity can be decomposed into geographical coordinate components from the given velocity u_r in $-\hat{e}_2$ direction:

$$l_2 = \sqrt{(\lambda'' - \lambda)^2 + \Delta\phi^2} \tag{4.12}$$

$$\hat{e}_2 = \frac{1}{R_E l_2}\vec{e}_2 \tag{4.13}$$

$$a_2 = (\vec{v}_{ExB} \cdot \hat{e}_2)\hat{e}_2 \cdot \hat{G}_E = u_r \frac{\Delta\phi}{l} \tag{4.14}$$

$$b_2 = (\vec{v}_{ExB} \cdot \hat{e}_2)\hat{e}_2 \cdot \hat{G}_N = u_r \frac{\lambda'' - \lambda}{l} \tag{4.15}$$

Each vector component sum

$$v_x = (a_1 + a_2)\hat{G_E} \tag{4.16}$$

$$v_y = (b_1 + b_2)\hat{G_N} \tag{4.17}$$

become the ion velocity components in the geographic east and north directions, respectively (Fig. 4.3(b)).

$$\begin{bmatrix} v_x \\ v_y \end{bmatrix} = \begin{bmatrix} a_1 & a_2 \\ b_1 & b_2 \end{bmatrix} \begin{bmatrix} u_z \\ -u_r \end{bmatrix} \tag{4.18}$$

4.4 Result

Fig. 4.6 is a map of the tangent unit vectors of Apex latitude on Cartesian coordinate on 1 January 2014, 00:15 UT at $h = 292.6$ km altitude. This height is the

nearest altitude to the desired 300 km in the data set. Contour lines are Apex latitudes drawn every 10°. The plot is drawn with unit vectors in grid every 10°for visibility. Figure 4.7 is a map of polar plot of the North Hemisphere. In both Figures 4.6-4.7 the color contours show the apex latitude ranging from 0°to 90°on a geographical grid. Blue arrows are unit tangent vectors $\hat{e}_1$ every 10 degrees in geographic coordinates. The arrows are all pointing eastward relative to the magnetic pole, which is easier to see in the polar plot of Figure 4.7. Note that at gridpoints at which an arrow is collocated with an apex latitude line, e.g., at $(\lambda, \phi) = (75°\text{N}, 130°\text{W})$ in Figure 4.6, the arrow is tangent to the Apex latitude contour. In Figure 4.7, an example point showing that the vector found is tangent to the apex latitude line is at $(\lambda, \phi) = (60°\text{N}, 160°\text{W})$.

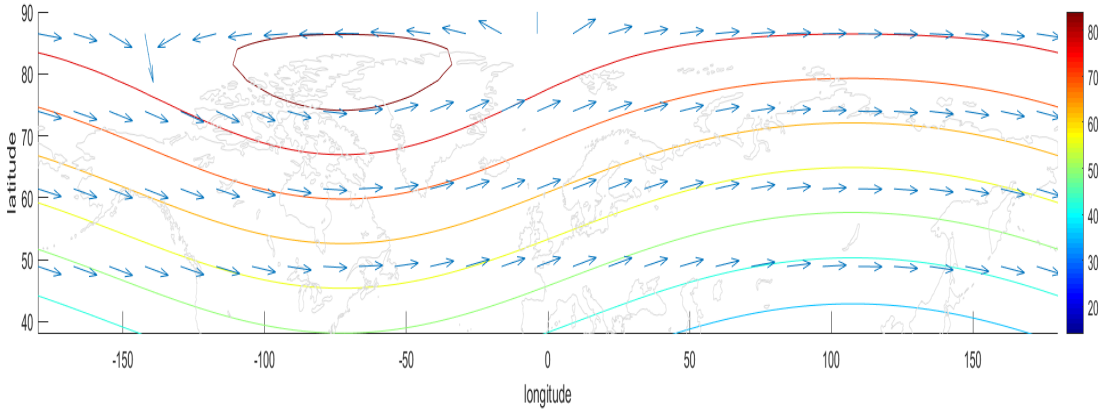

Figure 4.6. Tangent unit vectors of Apex latitude on Cartesian coordinate on 1 January 2014, 00:15 UT at h =292.6 km altitude. Contour line is Apex latitude drawn every 10°The plot is drawn with unit vectors in grid with every 10°for visibility.

Figures 4.8-4.9 are maps of the vectors tangent to Apex longitude as computed with the method described in Section 4.3. The Apex longitude lines have color ranging from -90°to 90°. Note that, since Eq. (4.2) defines ϕ_A from the arcsine, there is an ambiguity in the quadrant in which the angle lies. For this reason, on the left upper

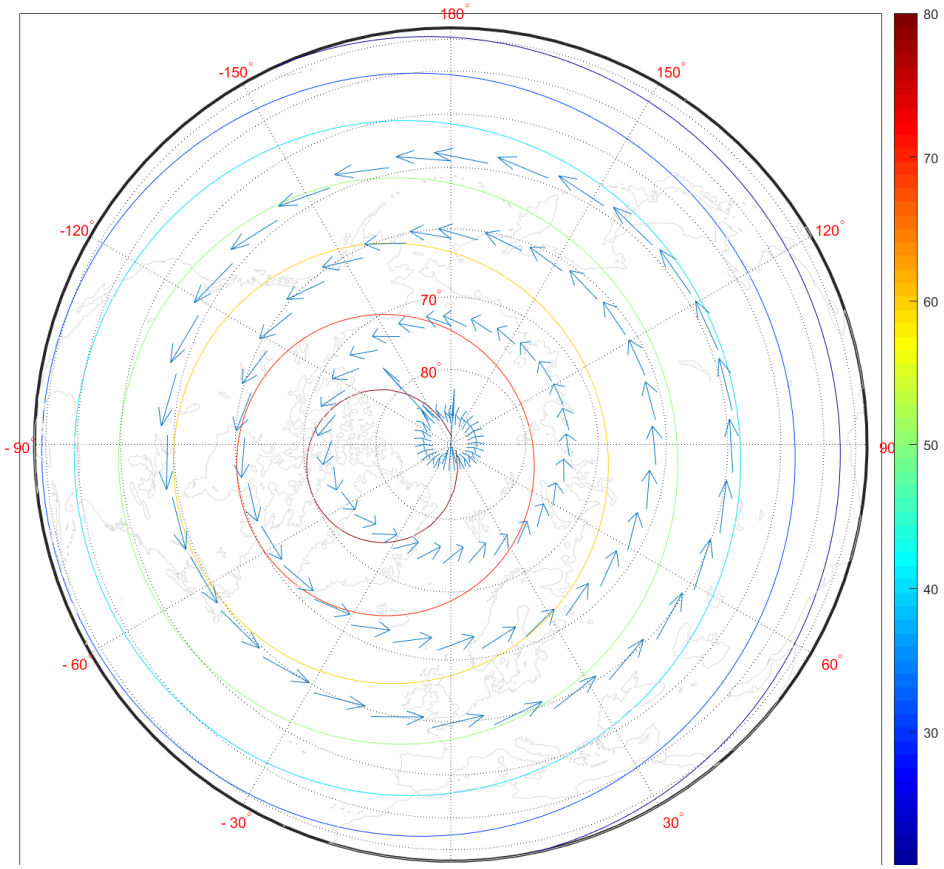

Figure 4.7. Maps of Apex latitude contours and tangent vectors at 292.6 km altitude on January 1st 2014 00:15UT on north polar plot. Apex latitude is shown as contour colors ranging from 0 to 90°, drawn every 10°for visibility. Blue arrows are unit vectors for each grid point, drawn every 10°.

part of the plot the lines range from 0°to -90°Apex longitude in color whereas the true Apex longitude range is -180°to -90°. A similar effect is also visible in the upper right part of the plot, in which the 90°to 0°color range corresponds to 90°to 180°in real Apex longitude range. However, since the purpose of plotting the apex longitude contour lines is to show that the tangent vectors are indeed tangent, the angle ambiguity does not need to be resolved.

Figure 4.10 is a plot of drift velocity components on a map of geographic longitude and latitude on 1 January 2014 00:15 UT at h =292.6 km altitude. Figure

4.11 is the same data on a polar plot of the northern hemisphere. The vectors are drift velocities transformed to the geographic coordinate directions. The typical high latitude $\vec{E} \times \vec{B}$ drift pattern is two cells of circulation, with flow from the noon longitude over the pole to midnight, then circulation around to the dawn longitude back to noon, and another around to the dusk longitude back to noon.

Since the time of this data set begins at t_0 =00:15 UT, local noon is at about 180°longitude. I expect the flow to point from 180°to 0°over the pole and divide into two cells of circulation around the dawn and dusk sides, converging at 180°longitude again. A simple cartoon of plasma drift streamlines with black arrows in Figure 4.11 shows a dusk circulation cell on the left half of the plot, as might be expected. However, streamlines on the right side of the North pole plot do not show uniform counter-clockwise circulation from midnight to dawn (90°longitude) to noon. Additional research correcting some of the simplifications is required for greater understanding.

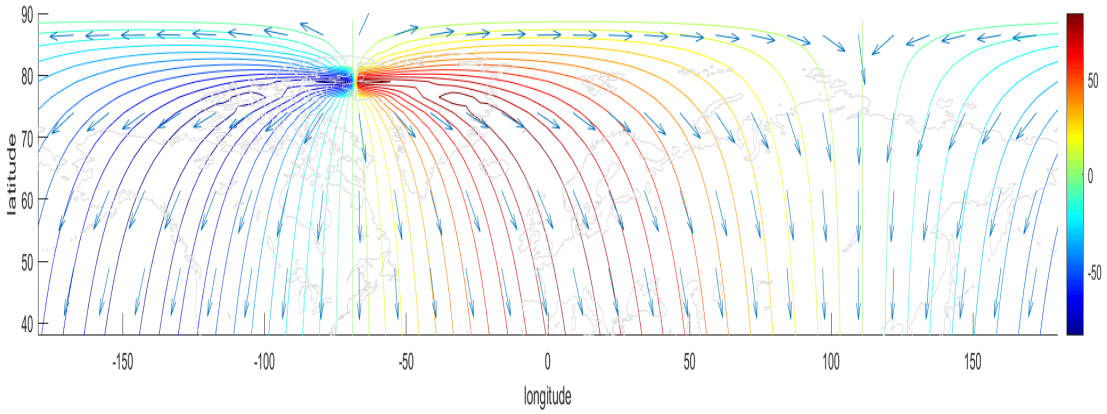

Figure 4.8. Tangent unit vectors of Apex longitude on 1 January 2014 00:15 UT at h =292.6 km altitude. Color contours are Apex longitude values with range -90°to 90°, drawn every 10°for visibility. The range of -180°to °-90 and 90°to °180 is not modified as we don't need the absolute apex value for finding tangent vector. Blue arrows are tangent vectors at 10 °geographic intervals, pointing equatorward.

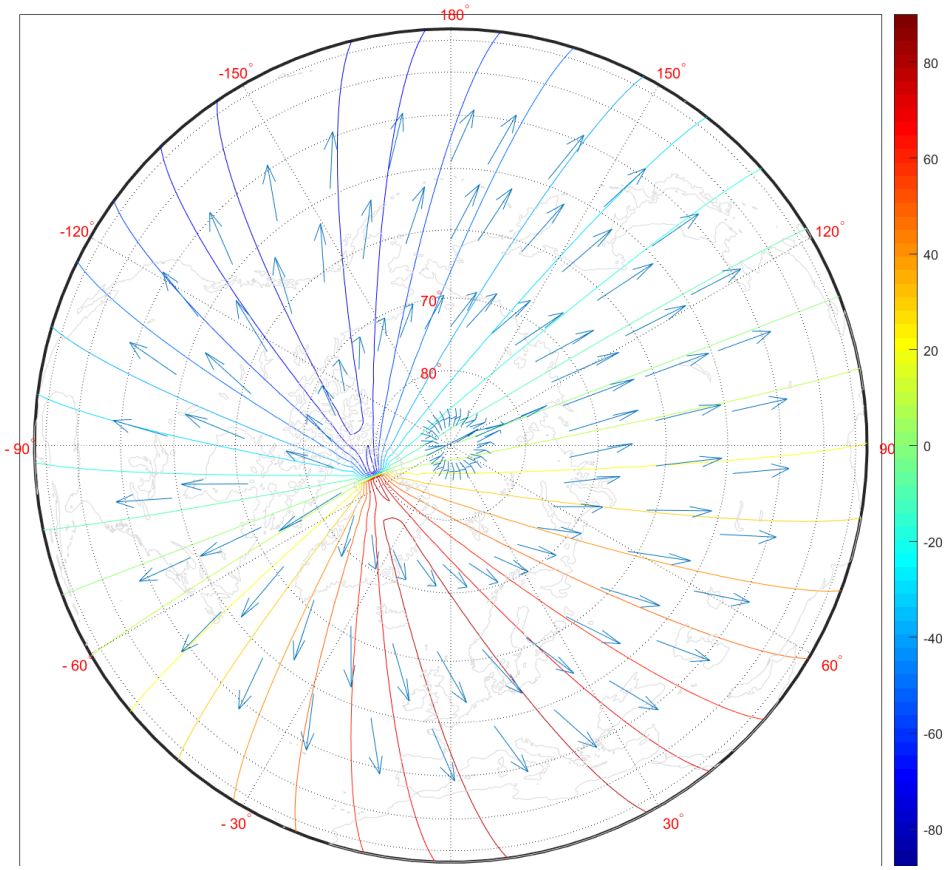

Figure 4.9. North pole plot of Apex longitude contours and the tangent vectors to Apex longitude. The plot is drawn with unit vectors pointing equatorward.

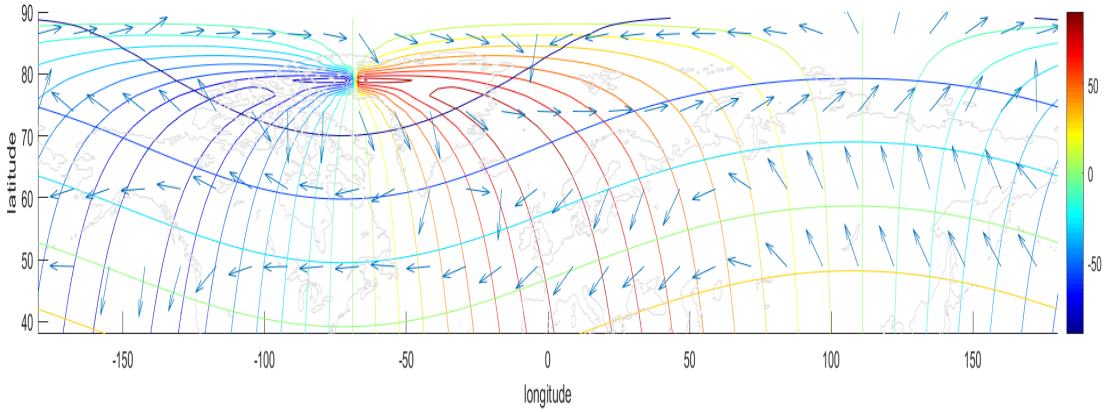

Figure 4.10. Vector sum of geographic drift velocity components on Cartesian coordinate on 1 January 2014 00:15 UT at h =292.6 km altitude. Color lines are Apex longitudes and latitudes in degrees. Blue arrows are drift velocity vectors at every 10°geographic grid.

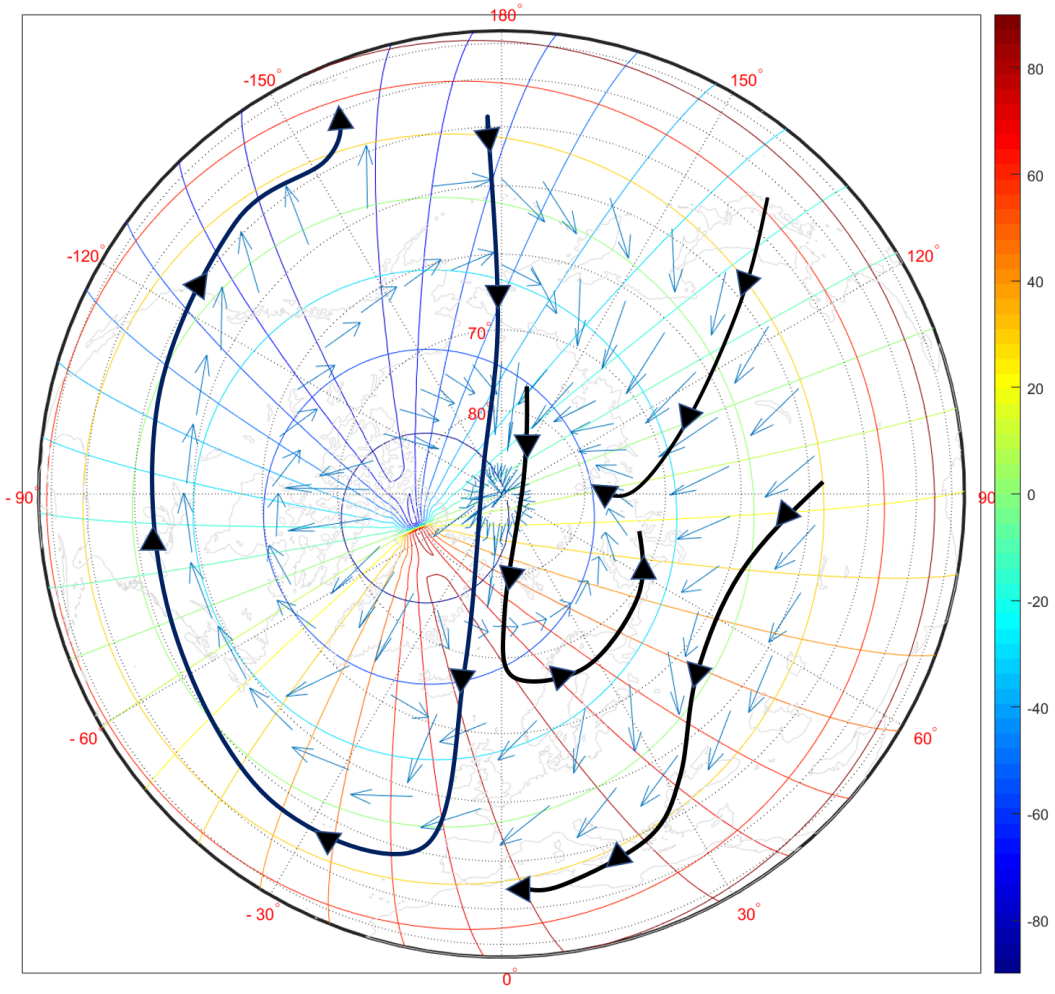

Figure 4.11. Same plot as Figure 4.10 seen from above the north pole. Black arrow lines are a simple cartoon of plasma velocity directions.

CHAPTER 5

USING POTENTIAL VALUE

To reduce runtime and possible errors in transformation, another method is investigated. Since the coordinate transformation in ion velocity includes the possible loss of accuracy in the vector transformation process due to simplifying assumptions made, rather than converting the coordinate components of vector velocities to geographic coordinates, here instead I calculate the $\vec{E} \times \vec{B}$ drifts directly from the SAMI3 electric potential values. This process is very similar to prior work, in which the electric potential value output by the Weimer model [9] was used to find LCSs [8].

The overall process can be seen in Figure 5.1. To obtain $\vec{E} \times \vec{B}$ drift, the external electric field and magnetic field must be modeled. The electric field can be found from the electric potential scalar field output from SAMI3. Writing the electric potential, V_E, again from Equation 2.8:

$$\vec{E} = -\vec{\nabla} V_E$$

The scalar potential value, V_E, is known. As the potential is scalar, its usage in $\vec{E} \times \vec{B}$ drift calculation is independent of unit vector coordinates chosen. The gradient can be computed in a user's desired vector coordinate system. The magnetic field $\vec{B}$ is given from the IGRF model mentioned in Section 2.2. Crossing the electric field and magnetic field vectors and dividing by the squared magnitude of the magnetic field, B^2, according to Equation 2.7 gives ion velocity vectors. These are converted to angular rates using Equations (2.18)-(2.19) before input to ITALCS for the FTLE calculation.

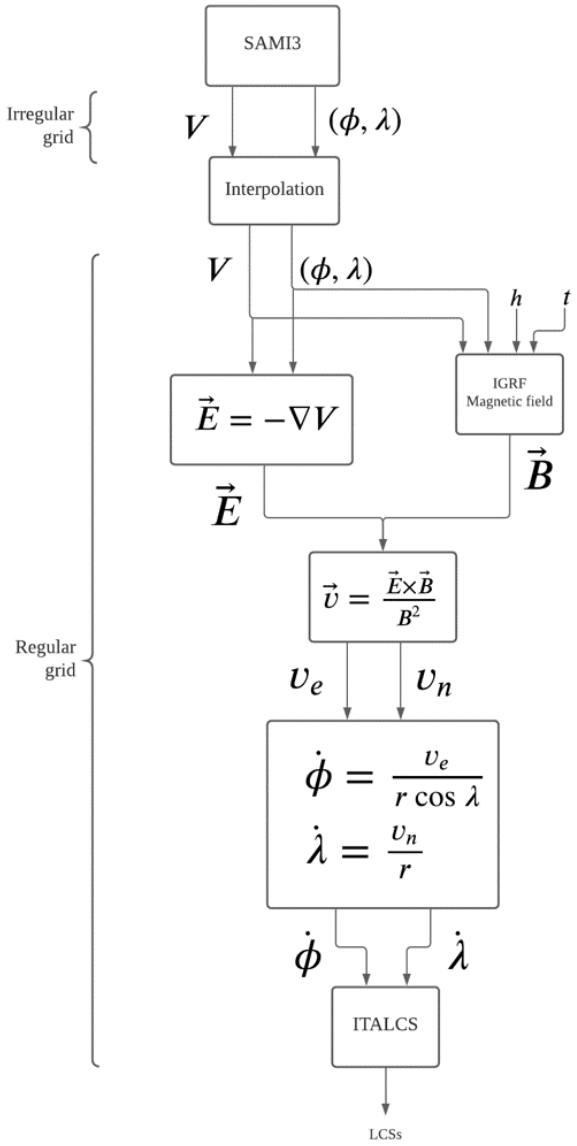

Figure 5.1. Overview of process for obtaining ionospheric LCSs using electric potential. Potential data given are on an irregular grid. To obtain a regular grid of velocities as required by ITALCS, interpolate the potential data to a regular grid. The $\vec{E} \times \vec{B}$ calculation takes the negative gradient of the potential, and crosses it with the IGRF magnetic field. After getting plasma velocity on a regular grid, expressed in geographic coordinates directions $\hat{G}_E, \hat{G}_N, \hat{G}_U$, the drift field can be input to ITALCS.

5.1 Interpolation and plotting

As mentioned in Section 2.5, the current version of ITALCS only accepts a regularly spaced grid of generalized coordinates (which may be latitude and longitude). However, the potential value from SAMI3 is provided on an irregular geographic grid. Therefore, before the $\vec{E} \times \vec{B}$ drift calculation, the electrical potential data of SAMI3 is interpolated onto a regular grid so that drift velocities can later be input to ITALCS on this grid.

The electric potential data is provided at 25 geographic latitudes between 40°to 90°, and at 51 geographic longitudes between -180°to 180°. The grid sparsity will impact the calculation of the gradient for electric field, and the propagation of particles for finding LCSs when used in ITALCS. So the data are spatially upsampled.

The MATLAB "cubic" interpolation method onto a 1°mesh grid is shown in Figure 5.2. The circles are the original potential values, and the mesh is the result based on 1 °grid interpolation. The map color range is potential and the vertical axis is kV. The horizontal axes are latitudes in the northern hemisphere and all longitudes.

The electric potential data sparsity in longitude appears to result in interpolation errors most visible as "valleys" in the high latitude high electric potentials (yellow). For example, the interpolation error "valley" is clearly shown in the area around (ϕ, λ) =(150°, 80°). We expect the highest potentials to smoothly vary with longitude at a single latitude.

The interpolation error leads to two problems with the output FTLE values from ITALCS. First, the production of "valleys" in the electric potential causes a zigzag pattern in a polar plot of the FTLE values output by ITALCS in Figure 5.3. Secondly, the interpolation does not span all the way to the 90°latitude or smoothly across the ±180°longitude boundary. As a result, electric potential data missing near

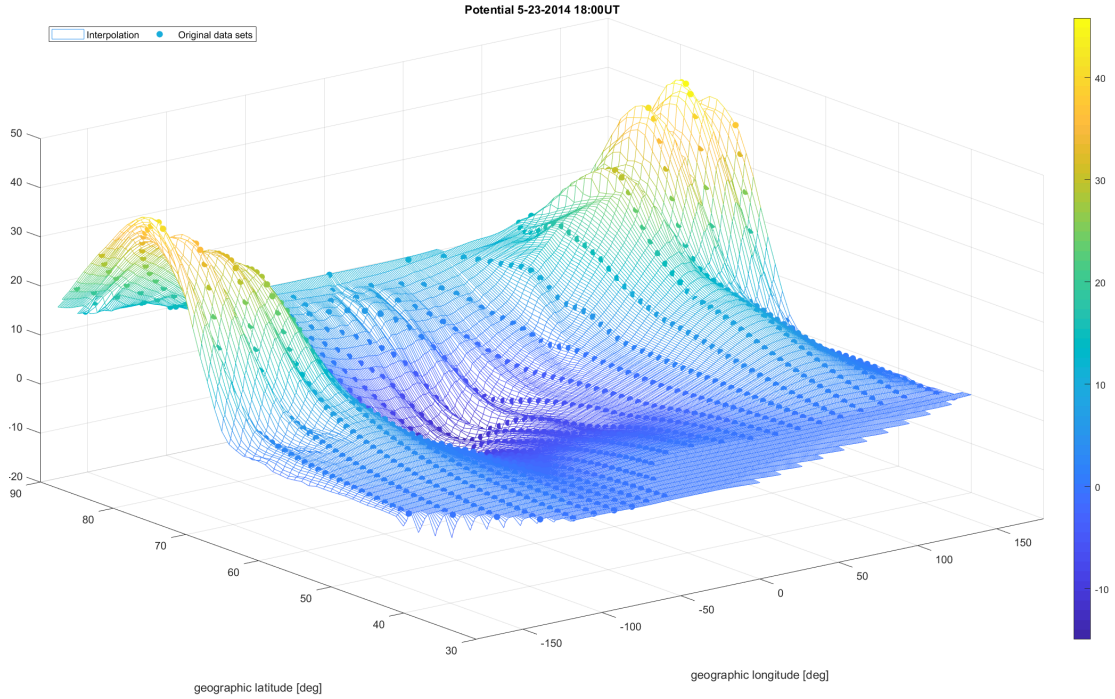

Figure 5.2. Electric potential (color and vertical axis) over latitude and longitude, interpolated from data provided at circles to a regular mesh. Result of 1°grid interpolation. The interpolation includes error in the form of valleys between the data points of highest potential.

the pole and 180°longitude leads to 0 FTLE values, spanning a wider spatial area as the integration time becomes longer in ITALCS (shown in Figure 5.4).

Those problems are reduced in the following ways. For the first problem (sparsity in longitude), the data are interpolated every 20°of geographic longitude, keeping the geographic latitude gap to 1°. This allows a smoother mesh plot as seen in Figure 5.5. However, the mesh data electric potential is smaller than values in the original data set at certain points, e.g., $(\phi, \lambda) = (150°$, latitude $80°)$, because interpolation is now occurring between the points provided, so the extrema are smoothed.

Missing data at the edge of longitude are recovered by repeating the data set periodically over the longitude intervals of [-200°, -180°], and [180°, 200°]. However,

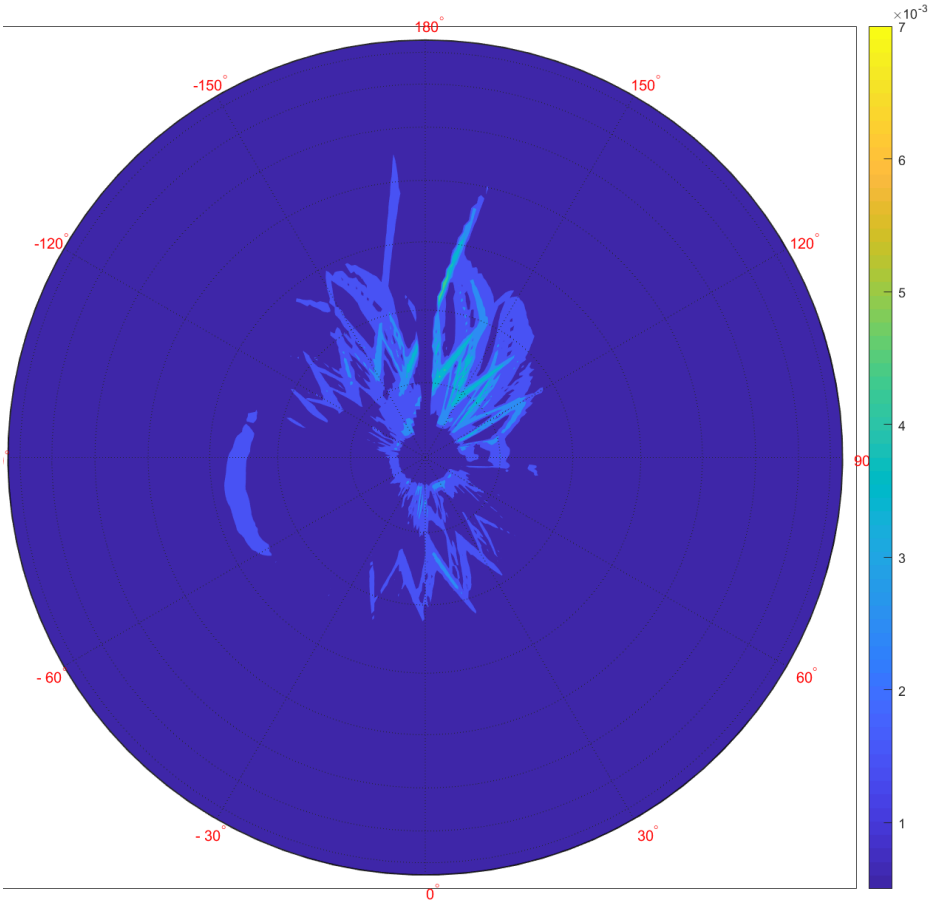

Figure 5.3. ITALCS Northern Hemisphere polar plot of FTLE values on 23 May 2014 18:00 UT. Integration time of $\tau = 10$ minutes. This polar plot shows the effect of interpolation errors and missing data on the resultant FTLE map.

missing data at the pole cannot be replaced without a more involved interpolation process. While the area missing FTLE values after running ITALCS decreases after solving the previous problems, as shown in Figure 5.6 and Figure 5.7, cumulative missing FTLE values still occur. To prevent FTLE values from becoming "not-a-number" (NaN) values from 88°to 90°latitude, I removed the velocity data poleward of latitude 87°.

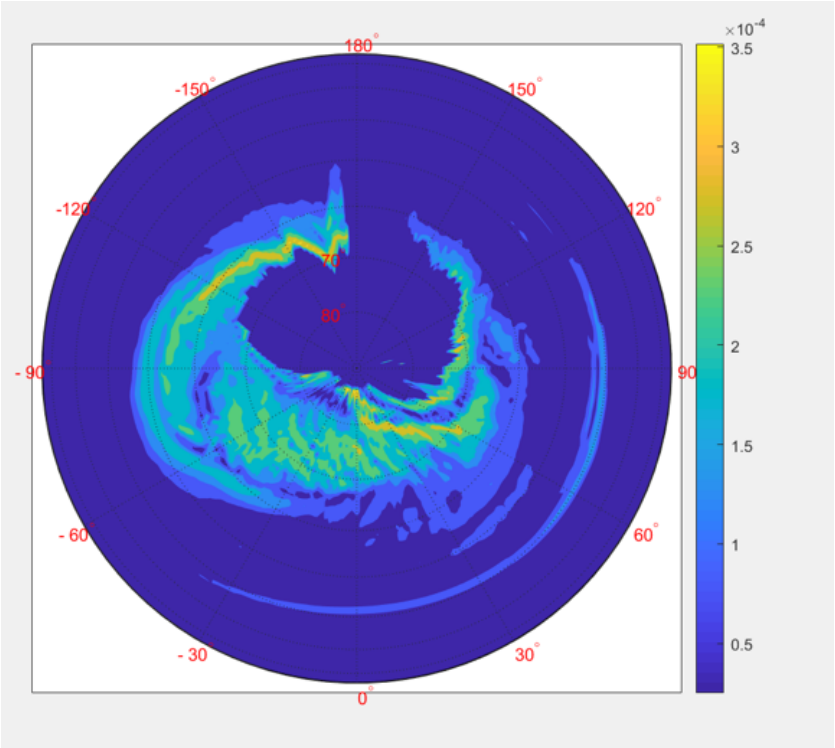

Figure 5.4. ITALCS Northern Hemisphere polar plot on 23 May 2014 18:00 UT. Integration time 1 hour, after interpolating to a coarser spatial grid.

5.2 Result

With the wider longitude grid for interpolation and accounting for spherical domain longitude periodicity and pole region, the FTLE map using ITALCS is shown in Figure 5.8. Tracer locations are computed by ITALCS for illustration. From the particles' movement in the northern hemisphere, LCSs can be interpreted by the three tracers. Three tracers A, B, C are initialized at A_0, B_0, C_0 and tracked over time, ending at A_f, B_f, C_f. Tracer C does not drift significantly. It is in a region of relatively low FTLE value. This means that the plasma drift and deformation is small. Tracers A and B are moving but in significantly different directions. This is indicated by the strong LCS ridge in yellow lying between A_0 and B_0 in Figure 5.8. Both tracers drift eastward, but then tracer A drifts strongly poleward. The LCS indicates deformation of particles as part of the flow turns poleward (as with tracer

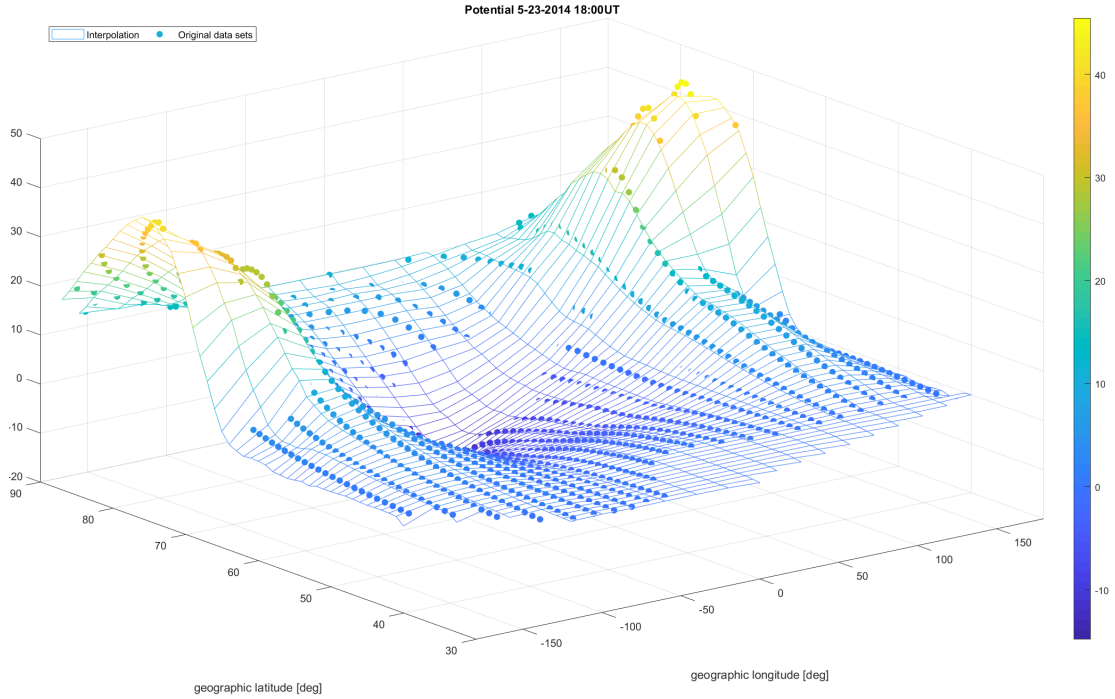

Figure 5.5. Result of interpolation to 20°longitude interval, 10°latitude interval grid. The interpolation errors causing multiple peaks and valleys in potential at 80°latitude has disappeared. However, the interpolation smooths out the peak values of the data, e.g., at the longitude 180°, latitude 85°area.

A) and part does not (as with tracer B). It appears that tracer A approaches the north geographic pole. Since the velocity data poleward of 88°was manually removed, I expect that for further integration time, the tracer will remain at the location A_f location.

Compared with the past research mentioned in background Section 2.5, the polar plot of the northern hemisphere has neither a horseshoe “U” shape nor a ”W” shape. However, the LCS ridge that appears is oriented on the day side as with the prior work. For an initial time of 18:00 UT, the local noon longitude is at -90°. This means the LCS ridge is centered in the local morning sector, which is comparable to the findings of prior work.

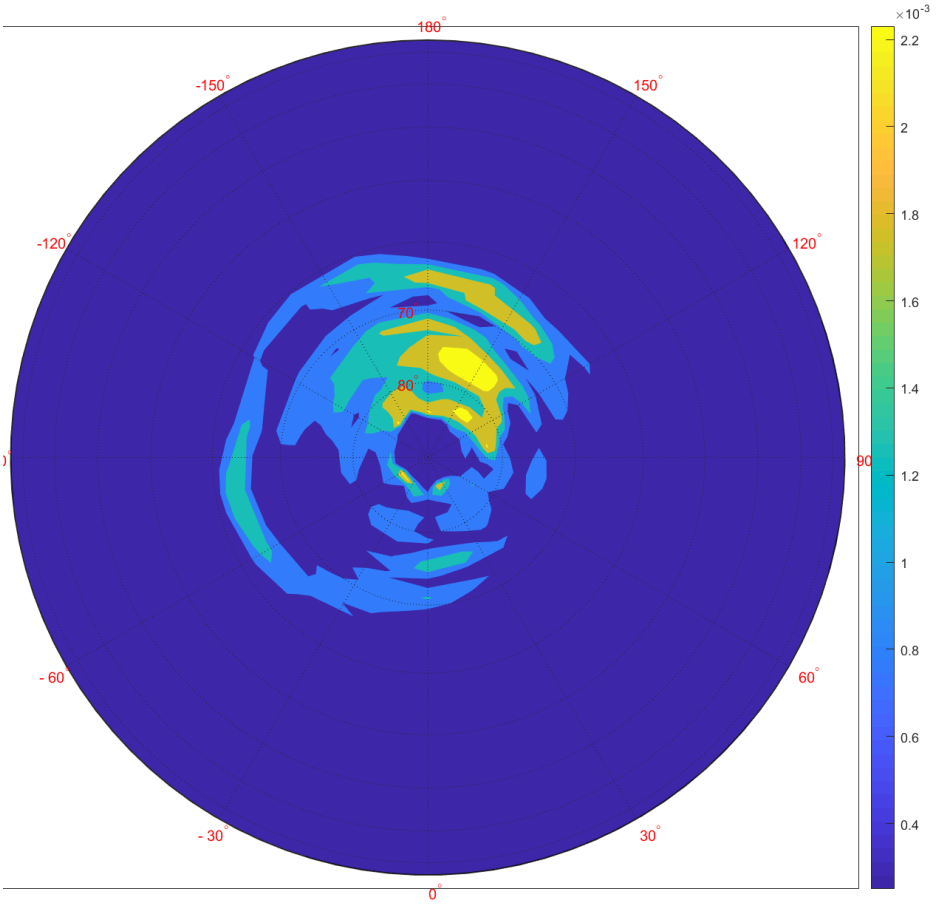

Figure 5.6. ITALCS Northern Hemisphere polar plot on 23 May 2014 18:00 UT. 10 minutes integration time. Improves upsampling error, but includes smoothing interpolation error of smaller potential value than the original data set, and missing data near the pole.

As SAMI3 is a first-principles ionospheric model, the result might be more representative of the ionospheric drift physics than previous work using ITALCS. On the other hand, significant smoothing due to interpolation in longitude occurred. Disconnected maximum FTLE values exist nearby the thickest LCSs, which might be a result of the wide data grid used in interpolation of the electric potentials.

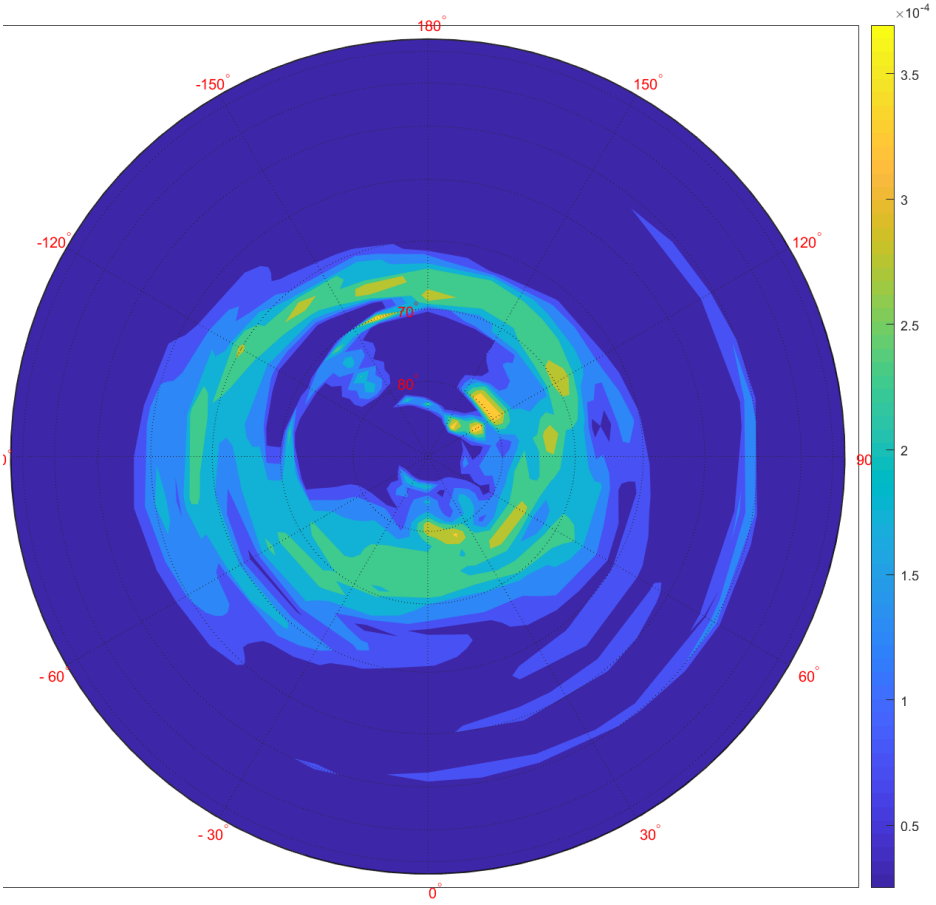

Figure 5.7. ITALCS Northern Hemisphere polar plot on 23 May 2014 18:00 UT. 1 hour integration time. Include errors of smaller potential value than original data set and missing data near the pole.

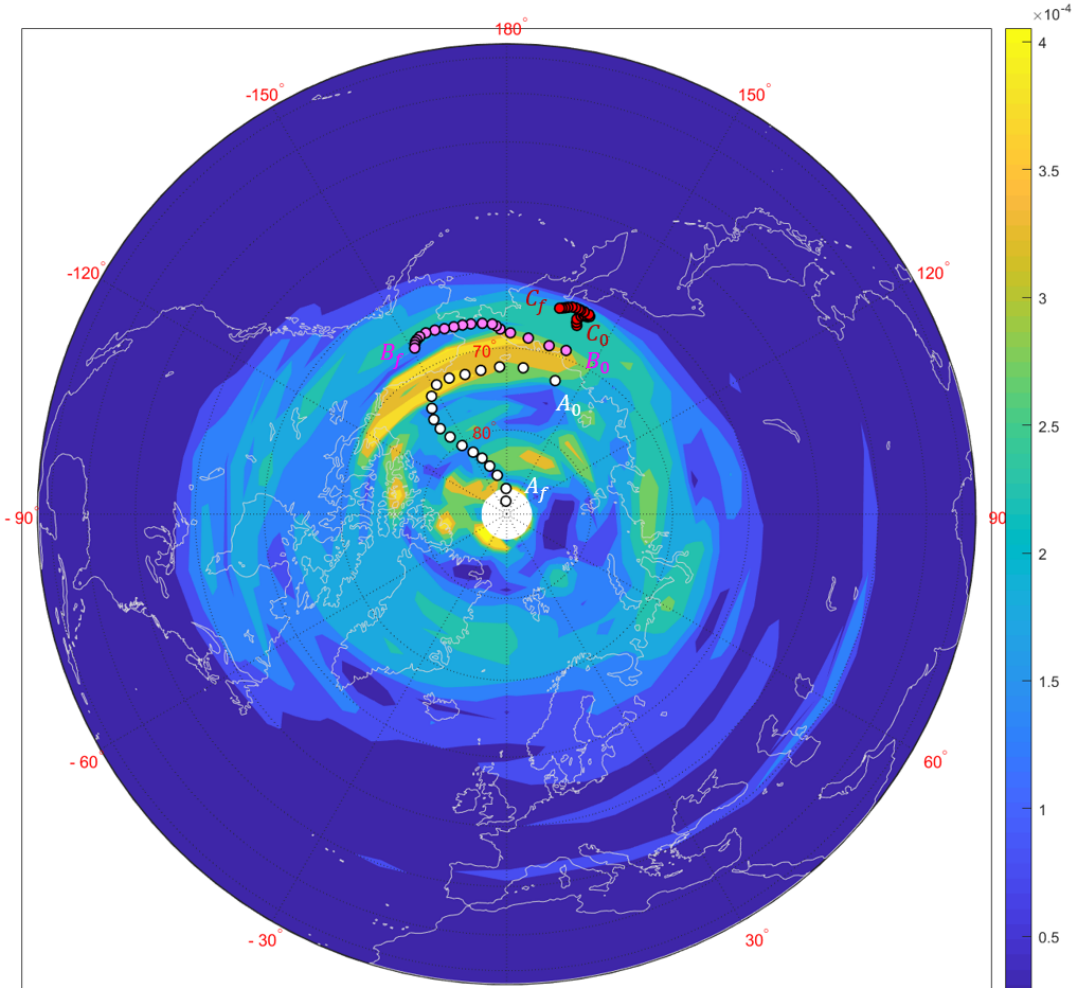

Figure 5.8. Maps of LCSs derived from SAMI3 potential over the northern hemisphere on 23 May 2014 18:00 UT, for 3 hours integration time. The color scale represents the FTLE values ranging from 0 to 4×10^{-4} s^{-1}. The initial longitude of tracers A_0, B_0, C_0 is $\phi = 160°$. Initial tracers A_0, B_0, C_0 are at latitudes λ of 73°, 69°, and 65°, respectively.

CHAPTER 6
CONCLUSION

6.1 Summary

This thesis produced the first map of high-latitude ionospheric Lagrangian coherent structures derived from a first-principles model of the ionosphere. In the process, the thesis explored three methods of preparing SAMI3 plasma drifts for input to the LCS computational tool ITALCS. Velocity fields input to ITALCS must be expressed in the same coordinate system as the gridpoints, and the gridpoints must be regularly spaced for ITALCS to compute the finite-time Lyapunov exponent (FTLE) field, whose maxima define the LCS. A geographic grid was desired for ease of interpretation of LCS location and for future comparison to polar cap patch observations.

Two of the methods explored transformations of vector quantities for different magnetic coordinate systems. The first method was a sequence of rotations between the orthogonal local magnetic coordinate system and geographic coordinates. The second method developed a way to construct tangent vectors from the non-orthogonal curvilinear coordinates that characterize the modified apex coordinates (the native grid of SAMI3). This method may help future researchers to work on vector rotations and non-orthogonal vectors transformations for future use for input to ITALCS.

The final and most successful method for obtaining the velocity components in the coordinates desired was to work directly with the electric potential output by SAMI3 (instead of the velocity components), then numerically compute the negative gradient and $\vec{E} \times \vec{B}$ drift in our coordinate system of choice (i.e., geographic). The LCS resulting from this approach was a dayside LCS at approximately the auroral

oval, but not one as extended as a full "horseshoe" shape, as prior studies using other models and data found.

6.2 Future Work

To potentially increase the accuracy of the curvilinear tangent vector estimation shown in Chapter 4:

- **Use the eccentric-dipole equation to find h_A:** As mentioned in Chapter 4, to confirm a simplified result, I used the centered dipole magnetic field model L-shell equation to find h_A. Although this allowed for verifying the method concept by distinguishing simple velocity vector directions, this assumption may lead to a distortion that affects data analysis. Therefore, I would argue that following the method but substituting in an eccentric-dipole expression to find h_A or directly using Apex coordinate calculator should significantly improve the accuracy. If an eccentric dipole expression is not readily available, a time-varying specification of the magnetic pole's coordinates (λ_0, ϕ_0) in Equations (4.2)-(4.3) should also improve the accuracy.

- **Use accurate λ_0 and ϕ_0 for 2014 data set:** While following the Apex longitude equation in paper , I used $\lambda_0 = 79°$N, $\phi_0 = 69°$W [20]. As of 2014 the magnetic pole is at approximately $\lambda_0 = 86°$and $\phi_0 = 206°$[21], which will result in different vector directions in Fig.4.11.

- **Consider spherical coordinate in tangent vector approximation:** From Eq.(4.6) -(4.7), the vector is applied based on the assumption of minimal $\delta\phi$ for tangent approximation. However, as the coordinate is based on spherical system, calculation considering without the assumption improve the result quality.

Several improvements can increase the completeness of the LCS maps made derived from the electric potential (from Chapter 5). These primarily relate to interpolation of the potential provided on an irregularly spaced geographic grid, to a regular latitude and longitude grid.

- **Higher resolutions ion velocity data to improve the plot accuracy:** Being provided an electric potential data set that enables interpolation over a grid with a less than 20°longitude gap will improve the resolution of the FTLE map.
- **Filling the missing data in pole region:** Recovering missing electric potential data in the polar region from 88°to 90°will improve the completeness of the FTLE map and the accuracy of tracer movement in ITALCS.
- **Improve interpolation:** Selecting or writing a new interpolation method will help to both keep peak potential values and smoothness between longitudes to increase the accuracy. A new interpolation may also help to provide interpolation over the pole.

Future work also includes comparing the LCS found for the 23 May 2014 event shown in Chapter 5 to observations of polar cap patches. A comparison of polar cap patches to LCSs in the winter hemisphere is part of future work, targeted for observations made in the years 2010 and 2014 [22].

BIBLIOGRAPHY

[1] J. A. Eddy, "The sun, the earth, and near-earth space: a guide to the sun-earth system." Washington, D.C.: National Aeronautics and Space Administration, 2009, p. 79.

[2] J. H. Meek, "Sporadic ionization at high latitudes," *Journal of Geophysical Research*, vol. 54, no. 4, pp. 339–345, Dec. 1949.

[3] D. Anderson and T. Fuller-Rowell. File:ionosphereprofilenoaa.png. [Online]. Available: https://commons.wikimedia.org/wiki/File:IonosphereProfileNOAA.png [Accessed: November 17, 2020].

[4] S. C. Shadden, F. Lekien, and J. E. Marsden, "Definition and properties of Lagrangian coherent structures from finite-time Lyapunov exponents in two-dimensional aperiodic flows," *Physica D: Nonlinear Phenomena*, vol. 212, no. 3-4, pp. 271–304, Dec. 2005.

[5] G. Haller, "Lagrangian Coherent Structures," p. 25, 2014.

[6] S. C. Shadden and A. Arzani, "Lagrangian Postprocessing of Computational Hemodynamics," *Annals of Biomedical Engineering*, vol. 43, no. 1, pp. 41–58, Jan. 2015.

[7] N. Wang, U. Ramirez, F. Flores, and S. Datta-Barua, "Lagrangian coherent structures in the thermosphere: Predictive transport barriers," *Geophysical Research Letters*, vol. 44, no. 10, pp. 4549–4557, May 2017.

[8] N. Wang, S. Datta-Barua, A. T. Chartier, U. Ramirez, and C. N. Mitchell, "Horseshoes in the High-Latitude Ionosphere," *Journal of Geophysical Research: Space Physics*, vol. 123, no. 7, pp. 5831–5849, Jul. 2018.

[9] D. R. Weimer, "Predicting surface geomagnetic variations using ionospheric electrodynamic models," *Journal of Geophysical Research*, vol. 110, no. A12, p. A12307, 2005.

[10] E. Thébault, C. C. Finlay, C. D. Beggan, P. Alken, J. Aubert, O. Barrois, F. Bertrand, T. Bondar, A. Boness, L. Brocco, E. Canet, A. Chambodut, A. Chulliat, P. Coïsson, F. Civet, A. Du, A. Fournier, I. Fratter, N. Gillet, B. Hamilton, M. Hamoudi, G. Hulot, T. Jager, M. Korte, W. Kuang, X. Lalanne, B. Langlais, J.-M. Léger, V. Lesur, F. J. Lowes, S. Macmillan, M. Mandea, C. Manoj, S. Maus, N. Olsen, V. Petrov, V. Ridley, M. Rother, T. J. Sabaka, D. Saturnino, R. Schachtschneider, O. Sirol, A. Tangborn, A. Thomson, L. Tøffner-Clausen, P. Vigneron, I. Wardinski, and T. Zvereva, "International Geomagnetic Reference Field: the 12th generation," *Earth, Planets and Space*, vol. 67, no. 1, p. 79, Dec. 2015.

[11] U. Ramirez, N. Wang, A. T. Chartier, and S. Datta-Barua, "SuperDARN Evidence for Convection-Driven Lagrangian Coherent Structures in the Polar Ionosphere," *Journal of Geophysical Research: Space Physics*, vol. 124, no. 5, pp. 3573–3588, May 2019.

[12] T. F. Tascione, "Introduction to the space environment." Malabar, FL: Krieger Publishing Company, 2010, pp. 4–5.

[13] J. A. Bittencourt, "Fundamentals of plasma physics." New York: Springer Verlag, 2004, p. 53.

[14] K. M. Laundal and A. D. Richmond, "Magnetic Coordinate Systems," *Space Science Reviews*, vol. 206, no. 1-4, pp. 27–59, Mar. 2017.

[15] Sami3 low-to-mid-latitude ionosphere. [Online]. Available: https://ccmc.gsfc.nasa.gov/models/modelinfo.php?model=SAMI3 [Accessed: March 15, 2020].

[16] J. D. Huba, G. Joyce, and J. A. Fedder, "Sami2 is Another Model of the Ionosphere (SAMI2): A new low-latitude ionosphere model," *Journal of Geophysical Research: Space Physics*, vol. 105, no. A10, pp. 23 035–23 053, Oct. 2000.

[17] "Coherent flow structures at earth's surface," J. G. Venditti, Ed. Chichester, West Sussex ; Hoboken, NJ: Wiley Blackwell, 2013, p. 1.

[18] E. NASA and A. S. G. S. F. Center). (21 April 2014) Jupiter and its shrunken great red spot. [Online]. Available: https://commons.wikimedia.org/wiki/File:Jupiter_and_its_shrunken_Great_Red_Spot.jpg [Accessed: November 15, 2020].

[19] A. D. Richmond, "Ionospheric Electrodynamics Using Magnetic Apex Coordinates." *Journal of geomagnetism and geoelectricity*, vol. 47, no. 2, pp. 191–212, 1995.

[20] T. E. VanZandt, W. L. Clark, and J. M. Warnock, "Magnetic apex coordinates: A magnetic coordinate system for the ionospheric F_2 layer," *Journal of Geophysical Research*, vol. 77, no. 13, pp. 2406–2411, May 1972.

[21] N. C. for Environmental Information. Wandering of the geomagnetic poles. [Online]. Available: https://www.ngdc.noaa.gov/geomag/GeomagneticPoles.shtml [Accessed: November 17, 2020].

[22] A. T. Chartier, C. N. Mitchell, and E. S. Miller, "Annual Occurrence Rates of Ionospheric Polar Cap Patches Observed Using Swarm," *Journal of Geophysical Research: Space Physics*, 2018.